Journal of Atmospheric and Solar–Terrestrial Physics 162 (2017) 28–47

Contents lists available at ScienceDirect

Journal of Atmospheric and Solar–Terrestrial Physics

journal homepage: www.elsevier.com/locate/jastp

Two-dimensional Morlet wavelet transform and its application to wave recognition methodology of automatically extracting two-dimensional wave packets from lidar observations in Antarctica

Cao Chen*, Xinzhao Chu*

Cooperative Institute for Research in Environmental Sciences & Department of Aerospace Engineering Sciences, University of Colorado Boulder, 216 UCB, CIRES, Boulder, CO 80309, USA

ARTICLE INFO

Keywords:
2-D wavelet transform
Wave pattern recognition
Persistent inertia-gravity waves
Antarctic lidar observation

ABSTRACT

Waves in the atmosphere and ocean are inherently intermittent, with amplitudes, frequencies, or wavelengths varying in time and space. Most waves exhibit wave packet-like properties, propagate at oblique angles, and are often observed in two-dimensional (2-D) datasets. These features make the wavelet transforms, especially the 2-D wavelet approach, more appealing than the traditional windowed Fourier analysis, because the former allows adaptive time-frequency window width (i.e., automatically narrowing window size at high frequencies and widening at low frequencies), while the latter uses a fixed envelope function. This study establishes the mathematical formalism of modified 1-D and 2-D Morlet wavelet transforms, ensuring that the power of the wavelet transform in the frequency/wavenumber domain is equivalent to the mean power of its counterpart in the time/space domain. Consequently, the modified wavelet transforms eliminate the bias against high-frequency/small-scale waves in the conventional wavelet methods and many existing codes.

Based on the modified 2-D Morlet wavelet transform, we put forward a wave recognition methodology that automatically identifies and extracts 2-D quasi-monochromatic wave packets and then derives their wave properties including wave periods, wavelengths, phase speeds, and time/space spans. A step-by-step demonstration of this methodology is given on analyzing the lidar data taken during 28–30 June 2014 at McMurdo, Antarctica. The newly developed wave recognition methodology is then applied to two more lidar observations in May and July 2014, to analyze the recently discovered persistent gravity waves in Antarctica. The decomposed inertia-gravity wave characteristics are consistent with the conclusion in Chen et al. (2016a) that the 3–10 h waves are persistent and dominant, and exhibit lifetimes of multiple days. They have vertical wavelengths of 20–30 km, vertical phase speeds of 0.5–2 m/s, and horizontal wavelengths up to several thousands kilometers in the mesosphere and lower thermosphere (MLT). The variations in the extracted wave properties from different months in winter indicate a month-to-month variability in the gravity wave activities in the Antarctic MLT region.

1. Introduction

Observing and characterizing the field of atmospheric waves across various temporal and spatial scales has been, and continues to be, one of the most challenging tasks in atmospheric and space science research. Waves are the dominant mechanism for energy and momentum transport in the middle and upper atmosphere. Characterizing them is critically important to the understanding of circulation in Earth's atmosphere and ensuring the accuracy of numerical models that are used for climate prediction and weather forecasting. Advancements in remote sensing technologies in the last several decades have significantly improved the observing capabilities, providing volumes of data with unprecedented coverage, precision, and temporal and spatial resolutions. Efforts have been spent on analyzing the data to characterize the properties of various atmospheric waves, including gravity, tidal and planetary waves, by means of Fourier basis functions (e.g., Chu et al., 2011a; Forbes, 1995; Gardner and Voelz, 1987; Harris, 1994; Lu et al., 2015; Manson and Meek, 1986; Nakamura et al., 1993; Sato, 1994; She et al., 2004). However, because Fourier methods assume a time/space invariance of wave properties, more efforts are needed in the aspect of localization of these wave properties because, in reality, many waves are inherently intermittent and localized (Alexander and Dunkerton, 1999; Forbes et al., 1995; Sato and Yamada, 1994; Teitelbaum

* Corresponding authors.
E-mail addresses: Cao.Chen@Colorado.edu (C. Chen), Xinzhao.Chu@Colorado.edu (X. Chu).

http://dx.doi.org/10.1016/j.jastp.2016.10.016
Received 9 April 2016; Received in revised form 23 October 2016; Accepted 24 October 2016
Available online 27 October 2016
1364-6826/

and Vial, 1991), i.e., wave properties such as amplitude, frequency, and vertical wavenumber vary with both time and space as the wave propagates. Traditional Fourier analysis is not capable of resolving localized variations (Farge, 1992). Windowed Fourier transforms are capable of localization, but use a fixed window width for all wave frequencies (or wavenumbers, same hereinafter) (Daubechies, 1992), which cannot dynamically adjust to lower or higher frequency phenomena. In contrast, the wavelet transform is able to adapt its window's temporal width to the wave spectrum, i.e., automatically narrowing at high frequencies and widening at low frequencies (Chui, 1992). Therefore, wavelet analysis methods are more suitable than Fourier transform methods for analyzing real atmospheric wave phenomena.

Wavelets are a relatively new concept in applied mathematics but have gained fast development and diverse applications. The term originated in the field of geophysics in the early 1980s (Morlet et al., 1982a, 1982b) to describe seismic signals. Since then, significant advances in wavelet theory have been made. Wavelets have been used in quantum physics (Grossmann and Morlet, 1984; Paul, 1984), applied mathematics (Daubechies, 1988; Meyer and Salinger, 1993), signal processing (Mallat, 1989), image compression (Wickerhauser, 1994), atmospheric turbulence (Farge, 1992), ocean wind waves (Liu, 1994) and many other fields. Their advantage, in addition to the localization capability, is the existence of many compactly supported orthonormal wavelet bases which allow signal decomposition into a minimal number of coefficients, enabling data compression (Daubechies, 1988; Meyer, 1989). The 1-D wavelet has been popular for middle and upper atmospheric data analysis (e.g., Sato and Yamada, 1994; Zhang et al., 2001; Zink and Vincent, 2001; Pancheva et al., 2002). Recent lidar observations in Antarctica, assisted with the 1-D Morlet wavelet data analysis technique, have led to the discoveries of persistent gravity waves in the mesosphere and lower thermosphere (MLT) (Chen et al., 2016a). These findings are significant, as they provide a rare insight into a poorly understood part of the Earth's atmosphere.

While the 1-D wavelet analysis applied in Chen et al. (2016a) was instrumental in characterizing the persistent waves from time series at each individual altitude, discerning each wave feature across both the time and space domains had to be performed manually; a situation that is not desirable when handling large amounts of observational data. In addition, wave packets may travel “obliquely” and exist in different regions at different times. Such intrinsic features require spectral analyses of waves in more than one dimension simultaneously. Many remote sensing instruments deliver two-dimensional (2-D) data. For example, ground-based lidars and radars record space-resolved atmospheric data over time at a fix location, yielding 2-D data in the altitude-time domains. Ground-based imagers, and many satellite sensors, obtain snapshots of 2-D spatial images. Unfortunately, extracting intermittent/localized two-dimensional wave packets is still a common technical challenge in analyzing atmospheric and space data. Therefore, we believe that the 2-D wavelet transform is an important and powerful tool for the autonomous processing of atmospheric data. Although some studies have used the 2-D wavelet transforms (e.g., Farge et al., 1990; Kaifler et al., 2015; Kumar, 1995; Wang and Lu, 2010), no 2-D Morlet wavelet code suitable for geophysical applications is publicly available. Moreover, the mathematical formalism is lacking regarding the absolute power spectrum of the 2-D wavelet transforms and the quantified relationship between the scale parameters and the Fourier periods/wavelengths.

The main goals of this study are to establish the mathematical formalism of modified 1-D and 2-D Morlet wavelet transforms with proper physical basis, and to develop a wave recognition methodology based on such 2-D wavelet transform for automatic wave extraction. The wave recognition methodology can be made available to the public for the analysis of large amounts of 2-D atmospheric and space science datasets. The formalism of the 1-D and 2-D wavelet transforms is established with detailed mathematical derivations. During the application of the 1-D wavelet technique in Chen et al. (2016a), problems were found in the publicly available 1-D wavelet code provided by Torrence and Compo (1998), i.e., wavelet power spectra are distorted or biased in favor of large scales or low frequencies, as Liu et al. (2007) pointed out previously for atmosphere and ocean science applications. To overcome this issue, corrections were made to the code in Chen et al. (2016a), but no mathematical explanations were offered. In this study we provide the mathematical and physical basis for the correction to the 1-D wavelet in Section 2 to illustrate the procedure for constructing an unbiased wavelet transform mathematically and to offer physical meaning to the wavelet spectrum. We then expand this procedure to the development of 2-D wavelet transform in Section 3. In order to apply the 1-D and 2-D transforms to real observational data, the continuous wavelet transform (CWT) must be discretized. This study provides equations for the discrete-time CWT in Sections 2 and 3. The 2-D inverse wavelet transform for wave reconstruction in the time/space domain is given in Section 4. Section 5 introduces the wave recognition methodology based on the modified 2-D wavelet transform that can automatically extract 2-D quasi-monochromatic wave packets and derive their wave properties. To demonstrate this methodology, we apply it to real lidar data taken during 28–30 June 2014 at McMurdo Station and compare our results to the 1-D results shown in Chen et al. (2016a). Application of the 2-D wavelet transform to lidar data from May and July 2014 is shown to help the characterization of persistent gravity waves in Antarctica. Section 6 discusses the potential caveats and improvements in our methods and the possible sources of these persistent waves. Finally, we conclude this study by highlighting the scientific utility of the 2-D wavelet transforms.

2. Correction for commonly used one-dimensional wavelet power spectrum

The 1-D CWT is commonly defined as (Mallat, 1999)

$$W_{f\psi}(s,t)=\int_{-\infty}^{+\infty}f(t')\frac{1}{\sqrt{s}}\psi^{*}\left(\frac{t'-t}{s}\right)dt'=f(t)\otimes\frac{1}{\sqrt{s}}\psi^{*}\left(\frac{-t}{s}\right)=\frac{1}{2\pi}\int_{-\infty}^{+\infty}\hat{f}(\omega)\sqrt{s}\,[\hat{\psi}(s\omega)]^{*}e^{i\omega t}d\omega \tag{1}$$

where $f(t)$ is the function of interest, $\psi(t)$ is a wavelet mother function, s is the wavelet scale (usually restricted to positive numbers), operator $(^{*})$ denotes complex conjugate, operator $(\otimes)$ denotes convolution, and operator $(\hat{})$ denotes Fourier transform, i.e., $\hat{f}(\omega)=\int_{-\infty}^{+\infty}f(t)e^{-i\omega t}dt$ and $\hat{\psi}(\omega)=\int_{-\infty}^{+\infty}\psi(t)e^{-i\omega t}dt$. The factor $1/\sqrt{s}$ is to ensure wavelets $\frac{1}{\sqrt{s}}\psi(\frac{t}{s})$ are normalized, i.e., $\int_{-\infty}^{+\infty}\left|\frac{1}{\sqrt{s}}\psi(\frac{t}{s})\right|^{2}dt$ equals a constant and does not depend on s. Note that the third equality in Eq. (1) is a result of the convolution theorem, i.e., the Fourier transform of a convolution is the pointwise product of Fourier transforms, applying the inverse Fourier transform $f\otimes g=F^{-1}\{F(f)\cdot F(g)\}$. The wavelet scale s is proportional to the window width in a dilated wavelet $\psi(\frac{t'-t}{s})$. This property enables the wavelet “time-window” to dynamically adjust to higher or lower frequencies. The Morlet wavelet transform is provided to illustrate this feature and is defined as (Farge, 1992; Meyers et al., 1993; Weng and Lau, 1994),

$$\psi(t)=e^{i\omega_0 t}e^{-\frac{t^2}{2}}, \tag{2}$$

where $\omega_0 \geq 5$ in order to fulfill the "admissibility condition" that will be shown later in Eq. (3) (Farge, 1992). Note that some literatures include a normalization constant of $\pi^{-\frac{1}{4}}$ in their definition of Eq. (2) such that $\int_{-\infty}^{+\infty}|\psi(t)|^2dt = 1$ (e.g., Kumar and Foufoula-Georgiou, 1997; Morlet et al., 1982b; Torrence and Compo, 1998). However, such a constant is not a necessity in our definition here for two reasons. First, it is cancelled out if we do a forward wavelet transform (Eq. (1)) and then an inverse wavelet transform (shown later in Eq. (4)), so the value of this normalization constant will not affect the result of the reconstruction of wave packets. Second, the effect of this normalization constant on the wavelet analysis will be accounted for later in our definition of the wavelet power spectrum (Eq. (11)). Evaluating the wavelet transform given by Eq. (1) using the above-defined Morlet wavelet, we have $\psi^*(\frac{t'-t}{s}) = e^{-i\omega_0(\frac{t'-t}{s})}e^{-\frac{(t'-t)^2}{2s^2}}$. The Gaussian "window" in the Morlet wavelet, $e^{-\frac{(t'-t)^2}{2s^2}}$, varies its width with the wavelet scale s, so it is adaptive to both low and high frequency waves for wave localization. Note that s has the same dimension as t, i.e., time. The only constraint imposed on a real wavelet function $\psi(t)$ is the so called "admissibility condition" (Mallat, 1999),

$$C_\psi = \int_0^{+\infty}\frac{|\hat{\psi}(\omega)|^2}{\omega}d\omega < +\infty. \tag{3}$$

If $\psi(t)$ is admissible and real, the inverse wavelet transform, or wavelet synthesis, exists and is given by (Eq. (4.38) in Mallat, 1999),

$$f(t) = \frac{1}{C_\psi}\int_0^{+\infty}\int_{-\infty}^{+\infty}s^{-2}W_{f\psi}(s,t')\frac{1}{\sqrt{s}}\psi(\frac{t-t'}{s})dt'ds = \frac{1}{C_\psi}\int_0^{+\infty}\int_{-\infty}^{+\infty}s^{-2}\int_{-\infty}^{+\infty}f(t'')\frac{1}{\sqrt{s}}\psi^*(\frac{t''-t'}{s})dt''\frac{1}{\sqrt{s}}\psi(\frac{t-t'}{s})dt'ds. \tag{4}$$

The full derivation of Eq. (4) is provided in the Appendix A.1. If $\psi(t)$ is complex and $f(t)$ is real, e.g., Morlet wavelet, we should only take the real part of Eq. (4) (Daubechies, 1992)

$$f(t) = \frac{1}{C_\psi}\int_0^{+\infty}\int_{-\infty}^{+\infty}s^{-2}\Re\left[W_{f\psi}(s,t')\frac{1}{\sqrt{s}}\psi(\frac{t-t'}{s})\right]dt'ds, \tag{5}$$

where the admissibility condition changes to

$$C_\psi = \int_0^{+\infty}\frac{|\hat{\psi}(\omega)|^2+|\hat{\psi}(-\omega)|^2}{2\omega}d\omega = \int_{-\infty}^{+\infty}\frac{|\hat{\psi}(\omega)|^2}{2|\omega|}d\omega < +\infty. \tag{6}$$

It is worth analyzing the physical meaning of the wavelet transform of Eq. (1). If the variable t is time and ω is the corresponding angular frequency, then Parseval's theorem requires (Mallat, 1999)

$$\int_{-\infty}^{+\infty}|f(t)|^2dt = \frac{1}{2\pi}\int_{-\infty}^{+\infty}|\hat{f}(\omega)|^2d\omega. \tag{7}$$

Eq. (7) expresses the equality of the total energy of the signal in both time and spectral representations. Energy conservation applies to the wavelet transforms as well. The equivalent Parseval's theorem for the wavelet transform can be stated as (for full derivation of Eq. (8), see Appendix A.2)

$$\int_{-\infty}^{+\infty}|f(t)|^2dt = \frac{1}{C_\psi}\int_0^{+\infty}\int_{-\infty}^{+\infty}|W_{f\psi}(s,t)|^2\frac{1}{s}dt\frac{ds}{s}. \tag{8}$$

Traditionally, the squared amplitude of the wavelet transform $|W_{f\psi}(s,t)|^2$ has been used to describe the wavelet power spectrum, as in Torrence and Compo (1998). However, this definition is troublesome from a physical perspective, which can be shown in the following dimensional analysis. If the integrals in Eq. (7) and Eq. (8) are regarded as the total energy of signal $f(t)$, then $|f(t)|^2$ is the power, i.e., energy per unit time, while $|\hat{f}(\omega)|^2$ is the energy spectral density, i.e., energy per unit frequency. Because the right hand side of Eq. (8) is a double integral, $|W_{f\psi}(s,t)|^2$ is energy per unit time per unit frequency, which is power spectral density, equivalent to energy. Thus, $|W_{f\psi}(s,t)|^2$ does not represent the mean power of $f(t)$. The dimension of the signal's power ($|f(t)|^2$) equals the dimension of $|W_{f\psi}(s,t)|^2$ divided by the scale s. For a periodic signal $f(t)$, we can show mathematically below that the squared amplitude of the Morlet wavelet transform $|W_{f\psi}(s,t)|^2$ is proportional to s. Moreover, since $f(t)$ can be written as the sum of a series of cosine functions, $\hat{f}(\omega)$ can be written as a sum of Dirac delta functions.

$$\begin{aligned} f(t) &= \sum_{n=1}^{\infty}A_n cos(\omega_n t+\varphi_n),\\ \hat{f}(\omega) &= \sum_{n=1}^{\infty}\pi A_n[\delta(\omega-\omega_n)e^{i\varphi_n}+\delta(\omega+\omega_n)e^{-i\varphi_n}]. \end{aligned} \tag{9}$$

The squared amplitude of the Morlet wavelet transform for $f(t)$ is then

$$\begin{aligned} |W_{f\psi}(s,t)|^2 &= \left|\frac{1}{2\pi}\int_{-\infty}^{+\infty}\hat{f}(\omega)\sqrt{s}[\hat{\psi}(s\omega)]^*e^{i\omega t}d\omega\right|^2 = s\left|\frac{1}{2\pi}\int_{-\infty}^{+\infty}\hat{f}(\omega)\sqrt{2\pi}\cdot e^{\frac{-(s\omega-\omega_0)^2}{2}}e^{i\omega t}d\omega\right|^2\\ &= s\left|\frac{1}{2\pi}\int_{-\infty}^{+\infty}\sum_{n=1}^{\infty}\pi A_n[\delta(\omega-\omega_n)e^{i\varphi_n}+\delta(\omega+\omega_n)e^{-i\varphi_n}]\sqrt{2\pi}\cdot e^{\frac{-(s\omega-\omega_0)^2}{2}}e^{i\omega t}d\omega\right|^2\\ &= s\left|\frac{\sqrt{2\pi}}{2}\sum_{n=1}^{\infty}A_n\int_{-\infty}^{+\infty}[\delta(\omega-\omega_n)e^{i\varphi_n}+\delta(\omega+\omega_n)e^{-i\varphi_n}]\cdot e^{\frac{-(s\omega-\omega_0)^2}{2}}e^{i\omega t}d\omega\right|^2 = s\left|\frac{\sqrt{2\pi}}{2}\sum_{n=1}^{\infty}A_n\left[e^{\frac{-(s\omega_n-\omega_0)^2}{2}}e^{i\omega_n t}e^{i\varphi_n}+e^{\frac{-(s\omega_n+\omega_0)^2}{2}}e^{-i\omega_n t}e^{-i\varphi_n}\right]\right|^2. \end{aligned} \tag{10}$$

Eq. (10) shows that $|W_{f\psi}(s,t)|^2$ is proportional to s multiplied by an oscillating term. This explains why the wavelet power calculated in Torrence and Compo (1998) is distorted and biased in favor of large scales or low-frequency oscillations, as pointed out by Liu et al. (2007) and Chen et al. (2016a). To correct this bias, we divide $|W_{f\psi}(s,t)|^2$ by s and define an unbiased Morlet power spectrum as below,

$$P_f(s,t) = \frac{1}{C_\psi'^{\,2}}\frac{|W_{f\psi}(s,t)|^2}{s} = \frac{1}{C_\psi'^{\,2}}\left|\frac{1}{2\pi}\int_{-\infty}^{+\infty}\hat{f}(\omega)[\hat{\psi}(s\omega)]^* e^{i\omega t}d\omega\right|^2 = \frac{1}{C_\psi'^{\,2}}\left|\frac{1}{\sqrt{2\pi}}\int_{-\infty}^{+\infty}\hat{f}(\omega)e^{\frac{-(s\omega-\omega_0)^2}{2}}e^{i\omega t}d\omega\right|^2. \tag{11}$$

Note that this expression for the power spectrum was not rigorously derived from Eq. (8). It is a practical expression that still has the dimension of power but does not exhibit bias towards larger s. Following the methods of Meyers et al. (1993), the relationship between the equivalent Fourier period and the wavelet scale can be derived. By substituting $f(t)$ with a single cosine function $A_1 cos(\omega_1 t + \varphi_1)$ into Eq. (11), we find that $P_f(s,t)$ reaches its maximum at $s = \omega_0/\omega_1 = \omega_0 T_1/2\pi$, where T_1 is the period of the cosine function (see full derivation in Appendix A.3). Therefore, $s = \omega_0/\omega$ describes the relationship between s and the Fourier frequency ω of the wave. Further, C_ψ' in Eq. (11) can be chosen such that the wavelet power at $s = \omega_0/\omega_1$ equals the signal's mean power (averaged squared amplitude, $\frac{1}{T}\int_0^T |f(t)|^2 dt = \frac{1}{2}A_1^2$). As a result, we obtain $C_\psi' = \sqrt{\pi}$ for the 1-D Morlet wavelet power spectrum. For application to a real world signal that is sampled at discrete times, the CWT of such a discrete signal becomes,

$$W_{f\psi}(s,n) = \sum_{n'=0}^{N-1} f[n']\frac{1}{\sqrt{s}}\psi^*\left[\frac{n'-n}{s}\right]\Delta t = \frac{1}{N}\sum_{k=0}^{N-1}\hat{f}\left[\frac{2\pi k}{N\Delta t}\right]\sqrt{s}\left[\hat{\psi}[s\frac{2\pi k}{N\Delta t}]\right]^* e^{i\frac{2\pi kn}{N}}. \tag{12}$$

The discretization of t and ω is as follows: $t = n\Delta t$, where $n = 0, 1, 2...N\text{-}1$ and $\omega = 2\pi k/N\Delta t$, where $k = 0, 1, 2...N\text{-}1$. Function $f[n]$ is $f(t)$ sampled at discrete times $t = n\Delta t$ (brackets used to enclose the variables of a function denote the discrete functions). Once the wavelet is selected, we choose a set of scales s. For convenience, we can write s at level j as base 2 exponentials (Torrence and Compo, 1998):

$$s_j = s_0 2^{\frac{j}{J}}, \quad j = 0, 1, 2, 3, 4, \ldots, j_{max}, \tag{13}$$

where s_0 is the smallest resolvable scale, usually $2\Delta t$, j is an integer representing the level number, and J is the number of levels per octave. The discretized version of Eq. (11) is

$$P_f(j,n) = \left|\frac{1}{N}\sum_{k=0}^{N-1}\hat{f}\left[\frac{2\pi k}{N\Delta t}\right]\sqrt{2}\,e^{\frac{-\left(2^{j/J}s_0\frac{2\pi k}{N\Delta t}-\omega_0\right)^2}{2}}e^{\frac{2\pi ikn}{N}}\right|^2, \tag{14}$$

where the discrete Fourier transform is defined as $\hat{f}[k] = \sum_{n=0}^{N-1} f[n]exp(-\frac{i2\pi nk}{N})$.

To demonstrate the improvements of our method, we compare the above defined wavelet power spectrum results with those using the method in Torrence and Compo (1998) and the MATLAB wavelet toolbox program cwtft() with an arbitrary time series test case. The input time series is a summation of three sine waves with the same amplitude of 20 K but different periods (2 h, 8 h, 24 h, respectively, shown in Fig. 1a). The total length

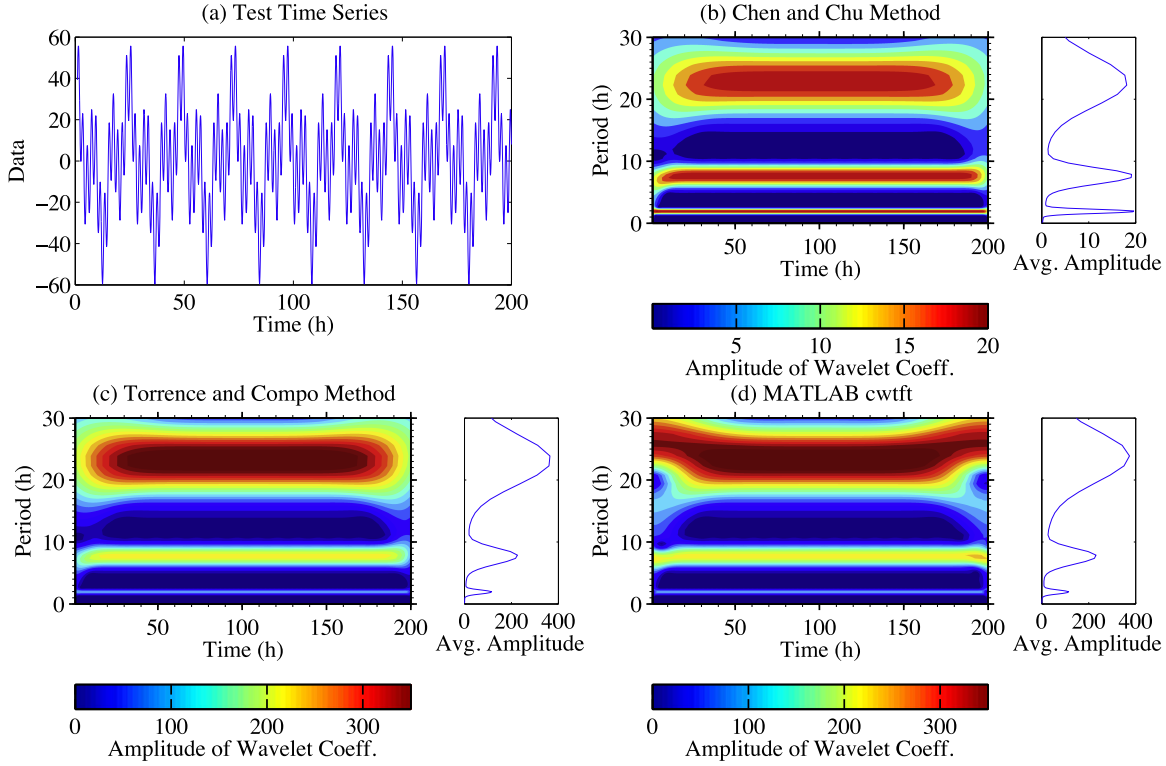

Fig. 1. 1-D Morlet wavelet power spectra of an (a) arbitrary test time series, calculated using (b) the Chen and Chu method, (c) the Torrence and Compo method, and (d) MATLAB program cftwt in the wavelet toolbox. The input time series is the summation of three sine waves with the same amplitude of 20 K but with different periods (2 h, 8 h, and 24 h respectively). For ease of comparison, time-averaged wavelet amplitudes are shown on the right of (b)–(d).

of the time series is 200 h with a sampling interval of 0.1 h. We use 101 levels for scale s, 10 per octave scale in the calculation, i.e., $j_{\max} = 100$ and $J = 10$ in Eq. (13). The Morlet wavelet power spectra calculated using the three different methods are shown in Fig. 1b–d. For easy comparison, time-averaged wavelet amplitudes are shown on the right of each panel. Our method yields the correct amplitude of 20 K for each wave without any bias. In contrast, the Torrence and Compo method and the MATLAB program produce similar results, which are both biased in favor of the longer period waves.

3. Two-dimensional Morlet wavelet power spectrum

1-D wavelet can be extended to two or more dimensions by rotation, dilation and translation (Murenzi, 1989). The 2-D CWT is defined as,

$$W_{f\psi}(s,\theta,\vec{t}) = \int_{-\infty}^{+\infty}\int_{-\infty}^{+\infty} f(\vec{t}\,')\frac{1}{s}\psi^*\left(\mathbf{\Omega}_\theta^{-1}\frac{\vec{t}\,'-\vec{t}}{s}\right)d\vec{t}\,' = f(\vec{t}\,)\otimes\frac{1}{s}\psi^*\left(\frac{-\mathbf{\Omega}_\theta^{-1}\vec{t}}{s}\right) = \frac{1}{4\pi^2}\int_{-\infty}^{+\infty}\int_{-\infty}^{+\infty} f(\vec{\omega})s[\psi(s\mathbf{\Omega}_\theta^{-1}\vec{\omega})]^* e^{i\vec{\omega}\cdot\vec{t}}d\vec{\omega}, \tag{15}$$

where $\vec{t} = (t, z)$, with t and z representing time and spatial coordinates, $\vec{\omega} = (\omega, m)$, with ω and m representing angular frequency and vertical wavenumber, respectively. Note that $d\vec{t} = dtdz$ and $d\vec{\omega} = d\omega dm$, and operator ($\otimes$) denotes the 2-D convolution defined as $f(x, y)\otimes g(x, y) = \int_{-\infty}^{+\infty}\int_{-\infty}^{+\infty} f(x', y')\cdot g(x-x', y-y')dx'dy'$. The rotation matrix $\mathbf{\Omega}_\theta$ is given below for a rotation parameter $\theta\in[0, 2\pi]$

$$\mathbf{\Omega}_\theta = \begin{pmatrix} cos\theta & -sin\theta \\ sin\theta & cos\theta \end{pmatrix}. \tag{16}$$

Eqs. (15) and (16) indicate that, in addition to expanding the dilations and translations used in the 1-D wavelet, rotations of $\vec{t}$ and $\vec{\omega}$ are introduced in the 2-D wavelet, where θ denotes the rotation angle. The 2-D Morlet wavelet function is defined as follows,

$$\psi(\vec{t}\,) = e^{i\vec{\omega_0}\cdot\vec{t}}e^{-\frac{\left|\vec{t}\right|^2}{2}}, \tag{17}$$

where $\vec{\omega}_0 = (\omega_0, 0)$ and, we choose $\omega_0 = 6$ for this implementation in order to fulfill the admissibility condition as in the 1-D case (Farge, 1992). $\vec{\omega}_0\cdot\vec{t}$ is the dot product of two vectors and $|\vec{t}\,|^2 = t^2 + z^2$ is the squared vector magnitude. The Fourier transform $\hat{\psi}(\vec{\omega})$ is,

$$\hat{\psi}(\vec{\omega}) = 2\pi e^{-\frac{\left|\vec{\omega}-\vec{\omega_0}\right|^2}{2}}. \tag{18}$$

If the 2-D wavelet function is admissible, then

$$C_\psi = \int_{-\infty}^{+\infty}\int_{-\infty}^{+\infty}\frac{|\hat{\psi}(\omega, m)|^2}{\omega^2+m^2}d\omega dm < +\infty. \tag{19}$$

The inverse 2-D wavelet transform is,

$$f(\vec{t}\,) = \frac{1}{C_\psi}\int_0^{2\pi}\int_0^{+\infty}\int_{-\infty}^{+\infty}\int_{-\infty}^{+\infty} s^{-3}W_{f\psi}(s,\theta,\vec{t}\,')\frac{1}{s}\psi(\mathbf{\Omega}_\theta^{-1}\frac{\vec{t}-\vec{t}\,'}{s})d\vec{t}\,'dsd\theta. \tag{20}$$

When $f(\vec{t}\,)$ is real, we take the real part of Eq. (19) and restrict $\theta\in[0, \pi]$:

$$f(\vec{t}\,) = \frac{1}{C_\psi}\int_0^{\pi}\int_0^{+\infty}\int_{-\infty}^{+\infty}\int_{-\infty}^{+\infty} s^{-3}\Re\left[W_{f\psi}(s,\theta,\vec{t}\,')\psi(\mathbf{\Omega}_\theta^{-1}\frac{\vec{t}-\vec{t}\,'}{s})\right]\frac{1}{s}d\vec{t}\,'dsd\theta, \tag{21}$$

where the admissibility condition becomes

$$C_\psi = \int_{-\infty}^{+\infty}\int_{-\infty}^{+\infty}\frac{|\hat{\psi}(\omega, m)|^2}{2(\omega^2+m^2)}d\omega dm < +\infty. \tag{22}$$

The derivations of Eq. (20) and Eq. (21) are provided in Appendices A.4 and A.5, respectively. The equivalent Parseval's theorem for the 2-D wavelet transform is (for derivation, see Appendix A.6),

$$\int_{-\infty}^{+\infty}\int_{-\infty}^{+\infty}|f(\vec{t}\,)|^2 d\vec{t} = \frac{1}{C_\psi}\int_0^{2\pi}\int_0^{+\infty}\int_{-\infty}^{+\infty}\int_{-\infty}^{+\infty}|W_{f\psi}(s,\theta,\vec{t}\,)|^2\frac{1}{s^2}d\vec{t}\frac{ds}{s}d\theta. \tag{23}$$

Following the same logic as in the dimensional analysis of the 1-D case, we find that the dimension of $|f(\vec{t}\,)|^2$ equals the dimension of $|W_{f\psi}(s,\theta,\vec{t}\,)|^2$ divided by the scale s^2. Therefore, we define the 2-D Morlet wavelet power spectrum as,

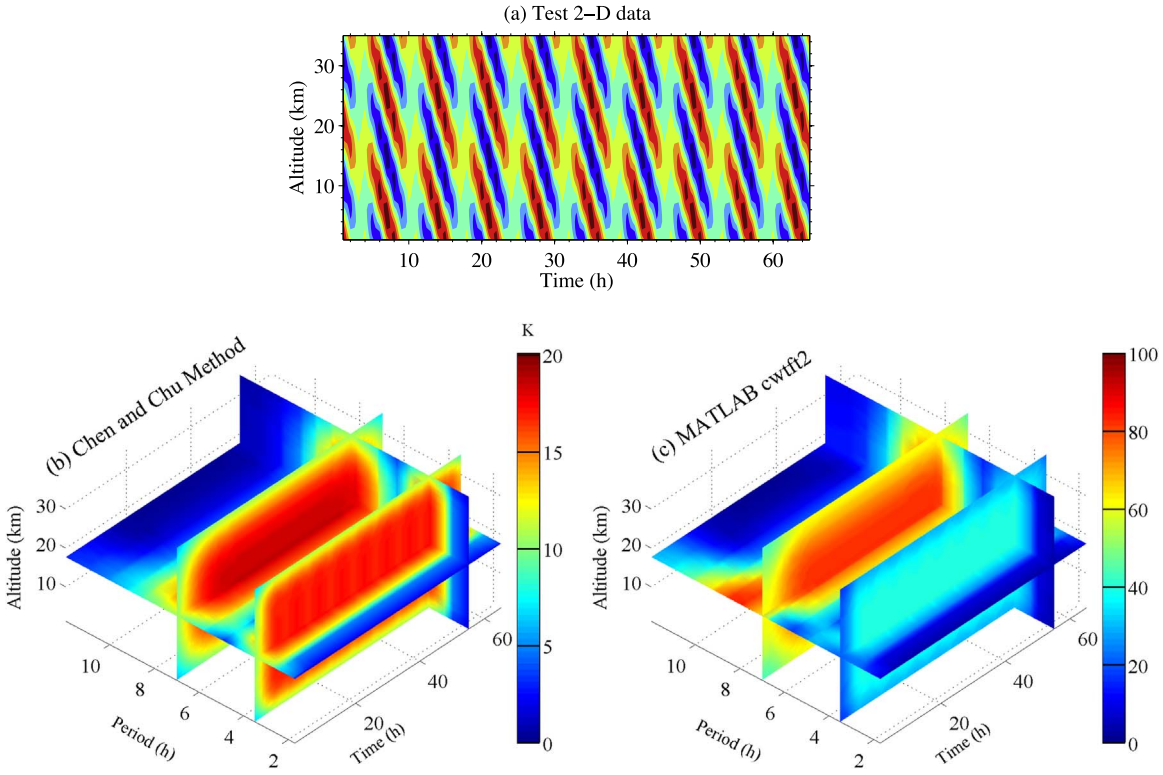

Fig. 2. Three-dimensional (3-D) illustration (coordinate λ_z fixed at 20 km) of the 2-D Morlet wavelet power spectrum of (a) an arbitrary test 2-D data set, comprised of two 2-D sine waves, with the same 20 km λ_z, the same 20 K amplitude, but different periods (3.5 h and 7 h, respectively), calculated using (b) the Chen and Chu method (Eq. (27)), and (c) MATLAB program cwtft2 in the wavelet toolbox. Four slice planes for each 3-D plots are at t = 55 h, z = 17.5 km, and T = 3.5 h and 7 h, respectively.

$$P_f(s,\theta,\vec{t}) = \frac{1}{C_\psi'^2}\frac{|W_{f\psi}(s,\theta,\vec{t})|^2}{s^2} = \frac{1}{C_\psi'^2}\frac{\left|\frac{1}{4\pi^2}\int_{-\infty}^{+\infty}\int_{-\infty}^{+\infty} f(\vec{\omega})s[\psi(s\Omega_\theta^{-1}\vec{\omega})]^* e^{i\vec{\omega}\cdot\vec{t}}d\vec{\omega}\right|^2}{s^2} = \frac{1}{C_\psi'^2}\left|\frac{1}{4\pi^2}\int_{-\infty}^{+\infty}\int_{-\infty}^{+\infty} f(\vec{\omega})2\pi e^{\frac{-|s\Omega_\theta^{-1}\vec{\omega}-\vec{\omega}_0|^2}{2}} e^{i\vec{\omega}\cdot\vec{t}}d\vec{\omega}\right|^2$$
$$= \frac{1}{C_\psi'^2}\left|\frac{1}{2\pi}\int_{-\infty}^{+\infty}\int_{-\infty}^{+\infty} f(\vec{\omega})e^{\frac{-|s\vec{\omega}-\Omega_\theta\vec{\omega}_0|^2}{2}} e^{i\vec{\omega}\cdot\vec{t}}d\vec{\omega}\right|^2 = \frac{1}{C_\psi'^2}\left|\frac{1}{2\pi}\int_{-\infty}^{+\infty}\int_{-\infty}^{+\infty} f(\vec{\omega})e^{\frac{-|s\vec{\omega}-\vec{\omega}_0'(\theta)|^2}{2}} e^{i\vec{\omega}\cdot\vec{t}}d\vec{\omega}\right|^2, \quad (24)$$

where $\vec{\omega}_0'(\theta) = (\omega_0 cos\theta, \omega_0 sin\theta)$. Analytical relationships between parameters s, θ and $\vec{\omega} = (\omega, m)$ of the Morlet wavelet can be derived using a similar method as in the 1-D case by substituting $f(\vec{t})$ with a 2-D cosine functions $A_1 cos(\omega_1 t + m_1 z)$. The results show that $P_f(s,\theta,\vec{t})$ will reach its maximum where $s = \sqrt{\omega_0^2/(m_1^2+\omega_1^2)}$ and $\theta = tan^{-1}(m_1/\omega_1)$, which describe the analytical relationships between parameters (s,θ) and (ω, m) (See full derivation in Appendix A.7). We derive the coefficient C_ψ' by ensuring that the result of the 2-D Morlet wavelet power at corresponding peak s and θ is equal to the signal's mean power $\frac{1}{2}A_n^2$. Doing so, we obtain $C_\psi' = \sqrt{2}\pi$ for the 2-D Morlet wavelet power spectrum.For practical application to a 2-D sampled, discrete signal, the continuous 2-D Morlet wavelet transform becomes,

$$W_{f\psi}[s,\theta,n_1,n_2] = \sum_{n_1'=0}^{N_1-1}\sum_{n_2'=0}^{N_2-1}\left\{f[n_1',n_2']\frac{1}{s}e^{\frac{-i[\omega_0\Delta t(n_1'-n_1)cos\theta+\omega_0\Delta z(n_2'-n_2)sin\theta]}{s}-\frac{[\Delta t(n_1'-n_1)]^2+[\Delta z(n_2'-n_2)]^2}{2s^2}}\Delta t\Delta z\right\}$$
$$= \frac{1}{N_1N_2}\sum_{k_1=0}^{N_1-1}\sum_{k_2=0}^{N_2-1}\left\{\hat{f}\left[\frac{2\pi k_1}{N_1\Delta t},\frac{2\pi k_2}{N_2\Delta z}\right]s\cdot 2\pi e^{-\frac{\left(\frac{s2\pi k_1}{N_1\Delta t}-\omega_0 cos\theta\right)^2+\left(\frac{s2\pi k_2}{N_2\Delta z}-\omega_0 sin\theta\right)^2}{2}+2\pi i\left(\frac{k_1 n_1}{N_1}+\frac{k_2 n_2}{N_2}\right)}\right\} \quad (25)$$

The discretization is as follows: $t = n_1\Delta t$, where n_1 = 0, 1, 2...N_1-1, $z = n_2\Delta z$, where n_2 = 0, 1, 2...N_2-1. $\omega = 2\pi k_1/N\Delta t$, where k_1 = 0, 1, 2... N_1-1, and $m = 2\pi k_2/N\Delta z$, where k_2 = 0, 1, 2... N_2-1. As with the 1-D wavelet, we need to choose a set of s and θ. For convenience, we use the same discrete representation of s as in the 1-D case but a uniform grid for θ as below

$$s_j = s_0 2^{\frac{j}{J}}, \quad j = 0, 1, 2, 3, \ldots, j_{max}$$
$$\theta_l = l\pi/L, \quad l = 0, 1, 2, 3, \ldots, L \quad (26)$$

The discrete version of Eq. (24) can now be written as

$$P_f[j,\, l,\, n_1,\, n_2] = \left| \frac{\sqrt{2}}{N_1 N_2} \sum_{k_1=0}^{N_1-1} \sum_{k_2=0}^{N_2-1} \left\{ \hat{f}\,[\frac{2\pi k_1}{N_1 \Delta t},\, \frac{2\pi k_2}{N_2 \Delta t}] e^{-\frac{\left(\frac{j}{2J} s_0 2\pi k_1 / N_1 \Delta t - \omega_0 cos(\frac{l\pi}{L})\right)^2 + \left(\frac{j}{2J} s_0 2\pi k_2 / N_2 \Delta t - \omega_0 sin(\frac{l\pi}{L})\right)^2}{2} + 2\pi i \left(\frac{k_1 n_1}{N_1} + \frac{k_2 n_2}{N_2}\right)} \right\} \right|^2 \tag{27}$$

To demonstrate that the above-formalized 2-D Morlet wavelet power spectrum yields unbiased wave amplitude results, we test it with an arbitrary 2-D data set, and compare the results with that calculated using the 2-D wavelet MATLAB program cwtft2(). The input 2-D data set is comprised of two 2-D sine waves (shown in Fig. 2a), with the same λ_z of 20 km, the same amplitude of 20 K, but different periods (3.5 h and 7 h, respectively). The time length of the data is 65 h with temporal resolution of 0.1 h, and the altitude range is 35 km with spatial resolution of 1 km. The result of a 2-D wavelet power spectrum is a four-dimensional (4-D) array, with each dimension representing scale s, rotation angle θ, time t and altitude z, respectively. We use 71 levels for scale s (10 per octave scale) and 71 levels of rotation angle θ in the calculation, i.e., $j_{max} = 70$, $J = 10$, and $L = 70$ in Eq. (26). More levels will yield higher resolution in period and λ_z in the 2-D wavelet transform, but will increase computation time. According to the derived relationships between (s, θ) and (ω, m) for a monochromatic 2-D cosine wave $cos(\omega t + mz)$, which are $s = \sqrt{\omega_0^2/(m^2 + \omega^2)}$, $\theta = tan^{-1}(m/\omega)$, s and θ can be converted into period T and λ_z using

$$\lambda_z = \frac{2\pi}{m} = \frac{2\pi s}{\omega_0 sin\theta}, \tag{28}$$

$$T = \frac{2\pi}{\omega} = \frac{2\pi s}{\omega_0 cos\theta}. \tag{29}$$

Now, the four coordinates of the 4-D array are λ_z, T, t and z, respectively. When the signs of T and λ_z are the same, the wave phase is downward progressing; when they are different, the wave phase is upward progressing. Since it is not possible to illustrate the full 4-D arrays here, we fix one of the coordinates at λ_z = 20 km, and present the resultant 3-D arrays in Figs. 2b and c. Fig. 2b shows the 2-D Morlet wavelet power spectrum calculated using our formalism (Eq. (27)), while Fig. 2c shows the one using MATLAB program cwtft2(). To make the comparison easier, both figures are sliced by four planes at t = 55 h, z = 17.5 km, and T = 3.5 h and 7 h, respectively. Fig. 2b clearly shows that our method yields the correct amplitude of 20 K for both waves without any bias. However, the current publicly available MATLAB program cwtft2() produces a distorted result in Fig. 2c, with the 7-h wave amplitude higher than that of the 3.5-h wave.

4. Two-dimensional wavelet reconstruction

We can use the wavelet reconstruction to extract the original 2-D data within a desired frequency and wavenumber band. Reconstruction provides an opportunity to study the characteristics of a 2-D wave packet. Note that in mathematics the wavelet analysis and synthesis refer to the forward and inverse transform of wavelet, respectively. Farge (1992) has pointed out that the synthesizing wavelet function used in the inverse wavelet transform (the latter $\psi(t)$ in Eq. (4)) could be very different from the analyzing wavelet function (the first $\psi^*(t)$ in Eq. (4)). We can even choose a delta function $\delta(t)$ to reconstruct the signal. In order to do so, the constant C_ψ needs to be redefined. In a 1-D wavelet, if $f(t)$ is real and $\psi(t)$ is a Hermitian function (i.e., its complex conjugate is equal to the original function $\psi(t) = \psi^*(-t)$, as with the Morlet wavelet),

$$f(t) = \frac{1}{C_\delta} \int_0^{+\infty} \int_{-\infty}^{+\infty} s^{-2} \Re[W_{f\psi}(s,\, u)] \frac{1}{\sqrt{s}} \delta\left(\frac{t-u}{s}\right) du ds = \frac{1}{C_\delta} \int_0^{+\infty} \Re[W_{f\psi}(s,\, t)] \frac{1}{\sqrt{s}} \frac{ds}{s} \tag{30}$$

where

$$C_\delta = \int_{-\infty}^{+\infty} \frac{\hat{\psi}(\omega)}{2|\omega|} d\omega < +\infty. \tag{31}$$

For a 2-D wavelet as a Hermitian function, such as the 2-D Morlet wavelet,

$$\begin{aligned} f(\vec{t}) &= \frac{1}{C_\delta} \int_0^{\pi} \int_0^{+\infty} \int_{-\infty}^{+\infty} \int_{-\infty}^{+\infty} s^{-3} \Re[W_{f\psi}(s,\, \theta,\, \vec{u})] \frac{1}{s} \delta\left(\mathbf{\Omega}_\theta^{-1} \frac{\vec{t} - \vec{u}}{s}\right) d\vec{u}\, ds d\theta \\ &= \frac{1}{C_\delta} \int_0^{\pi} \int_0^{+\infty} \Re[W_{f\psi}(s,\, \theta,\, t)] \frac{1}{s} \frac{ds}{s} d\theta, \end{aligned} \tag{32}$$

where

$$C_\delta = \int_{-\infty}^{+\infty} \int_{-\infty}^{+\infty} \frac{|\hat{\psi}(\omega,\, k)|}{2\sqrt{\omega^2 + k^2}} d\omega dk < +\infty. \tag{33}$$

The discretized versions of the 1-D wavelet reconstruction Eq. (30) and the 2-D wavelet reconstruction Eq. (32) are

$$f[n] = \frac{1}{C_\delta} \sum_{j=0}^{J} \frac{\Re\{W_{f\psi}[j,\, n]\}}{2^{\frac{j}{2J}} \sqrt{s_0}} \cdot \frac{ln2}{J}, \tag{34}$$

$$f[n_1,\, n_2] = \frac{1}{C_\delta} \sum_{l=0}^{L} \sum_{j=0}^{J} \frac{\Re\{W_{f\psi}[j,\, l,\, n_1,\, n_2]\}}{2^{\frac{j}{J}} s_0} \cdot \frac{\pi ln2}{JL}. \tag{35}$$

To derive C_δ for a discrete wavelet function, Torrence and Compo (1998) substituted $f[n]$ in Eq. (34) with a time series of a δ function, such that $\delta[n] = 1$ at $n = 0$. Since the Fourier transform of $\delta[n]$ has the uniform spectrum $\hat{\delta}[k] = 1$, we reconstruct Eq. (34) at $n = 0$ to obtain C_δ for the 1-D wavelet reconstruction,

$$C_\delta = \frac{1}{\delta[0]} \sum_{j=0}^{J} \frac{\Re\{W_{f\psi}[j, 0]\}}{2^{\frac{j}{2J}}\sqrt{s_0}} \cdot \frac{ln2}{J} = \sum_{j=0}^{J} \Re\left[\frac{1}{N} \sum_{k=0}^{N-1} \sqrt{2\pi}\, e^{\frac{\left(2^{j/J} s_0 \frac{2\pi k}{N\Delta t} - \omega_0\right)^2}{2}} \right] \cdot \frac{ln2}{J}. \tag{36}$$

Similarly, by substituting a 2-D time series $f[n_1, n_2] = \delta[n_1, n_2]$ into Eq. (35), we obtain C_δ for the 2-D wavelet reconstruction,

$$C_\delta = \sum_{l=0}^{L} \sum_{j=0}^{J} \Re\left[\frac{1}{N_1 N_2} \sum_{k_1=0}^{N_1-1} \sum_{k_2=0}^{N_2-1} 2\pi e^{\frac{\left(\frac{j}{2^J} s_0 \frac{2\pi k_1}{N_1\Delta t} - \omega_0 cos(\frac{l\pi}{L})\right)^2 + \left(\frac{j}{2^J} s_0 \frac{2\pi k_2}{N_2\Delta t} - \omega_0 sin(\frac{l\pi}{L})\right)^2}{2}} \right] \cdot \frac{\pi ln2}{JL}. \tag{37}$$

5. Wave recognition methodology of automatically extracting two-dimensional wave packets from lidar data

Based on our 2-D wavelet analysis and synthesis described above, we develop a wave recognition methodology to automatically identify and extract wave packets from the lidar data collected at McMurdo, Antarctica and derive the wave parameters. Besides demonstrating the usage of the 2-D wavelet analysis and synthesis, we will also exemplify how to identify the major wave peaks and determine their extension from the 2-D wavelet analysis results, a key step to extracting wave packets. The data used here were taken by the University of Colorado lidar group during the McMurdo lidar observational campaign that has been active since December 2010. An upgraded Fe Boltzmann/Rayleigh temperature lidar (Chu et al., 2002; Wang et al., 2012) is operated from Arrival Heights Observatory (77.83°S, 166.67°E) through a joint effort between the United States Antarctic Program (USAP) and Antarctica New Zealand (AntNZ) (Chu et al., 2011b). The observations are year-round, weather permitting. Because of the Antarctic darkness, the winter lidar data contain very little solar background (Chu et al., 2011a). Combined with the highest Fe layer abundance in winter (Yu et al., 2012), the winter months (i.e., May through August) provide the highest resolution temperature measurements with the largest altitude coverage (Chen et al., 2013; Chu et al., 2011a). In this paper we select three cases to demonstrate our methods. One dataset spans 28–30 June 2014 and was studied in detail by Chen et al. (2016a) using the 1-D wavelet analysis methods. Here, this case is used as the baseline for the comparison of the 2-D and 1-D wavelet methods. The second and third cases are the lidar runs on 23–24 May 2014 and 16–18 July 2014, respectively, which are chosen due to their long observation periods and minimal data gap owing to favorable weather conditions as well as in the winter months different than June. These three cases also serve to illustrate the wave variability in winter.

The raw lidar data (photon counts) were recorded with resolutions of 1 min and 48 m, from which Fe temperatures in the MLT are derived at resolutions of 0.25 h and 0.5 km, with the sampling window shifted in steps of 0.1 h and 0.1 km. Relative temperature perturbations are calculated from the raw temperature data by subtracting the dataset-mean temperature at each altitude and dividing by the mean, such that slow varying background atmosphere is removed. Fig. 3a shows the calculated relative temperature perturbations on 28–30 June 2014. We then apply the 2-D Morlet wavelet transform to such relative temperature perturbations and calculate their power spectrum using Eq. (27). In the calculation, we use 71 levels of s, 10 per octave scale, and 71 levels of θ, so the resolutions in the wavelet period and λ_z are respectively ~0.5 h and 2.5 km at $T \sim 7$ h and $\lambda_z \sim 22$ km. The spectral noise floor induced by the lidar measurement errors is estimated using a Monte Carlo simulation method described as follows. We first construct 1000 Gaussian white-noise simulation data at each grid point of the measurement with a standard deviation equal to the measurement error at that grid point. Then we calculate the wavelet power spectra for each of the above constructed 1000 sets of 2-D simulation data using the exact same method as we do for the real temperature measurements. Finally, the spectral noise floor is estimated by taking the mean of these 1000 simulated noise spectra. The spectral noise floor obtained above is then subtracted from the measured wavelet power spectrum. The results are shown in Figs. 3b and c, where we fix one of the coordinates and present the resultant 3-D array. Fig. 3b shows the power spectrum at $\lambda_z = 25$ km, where the 3-D data is sliced by three orthogonal planes at $t = 55$ h in Universal Time (UT), $z = 90$ km, and $T = 7.6$ h, respectively. Note that the unit of the color bar is $(\%)^2$. Three major wave packets with periods $T \sim 7.6$ h, $T \sim 6.5$ h and $T \sim 3.4$ h, respectively, can be identified in Fig. 3b (location of each peak is marked with a red arrow). Fig. 3c shows the power spectrum at $T = 7.6$ h, where the 3-D data is sliced by three planes at $t = 55$ UT, $z = 90$ km, and $\lambda_z = 25$ km, respectively. The peak $\lambda_z \sim 25$ km is clearly shown in Fig. 3c. Here spectral leakage from the 6.5-h wave into this 7.5-h power spectrum is visible due to their closeness in period, but these two waves are clearly separated in time in the 2-D wavelet spectrum. Fig. 3d is the 2-D top view of Fig. 3b in the unit of wave amplitude (%) showing how the wave periods change with time at $z = 90$ km and $\lambda_z = 25$ km. This 2-D contour plot resembles the 1-D wavelet amplitude spectra shown in Fig. 4a in Chen et al. (2016a), which is reproduced here in Fig. 3e. Both plots exhibit quite similar patterns of wave period spectra at $z = 90$ km, which verifies the capability of the 2-D wavelet transform. The 2-D wavelet amplitude in Fig. 3d is smaller than the 1-D wavelet amplitude in Fig. 3e. This is because the amplitude of the 2-D wavelet spectrum represents only a finite λ_z band ($\lambda_z = 25$ km), which is different from the 1-D wavelet spectrum that includes contributions from all λ_z.

After calculating the 2-D wavelet power spectrum, we utilize a MATLAB program “imregionalmax()” in the MATLAB Image Processing Toolbox to search for regional maxima (local peaks), which have the highest value among their connected neighborhood elements. For such a 4-D array, we use 80-connected neighborhoods for the search. We sort the regional maxima according to their peak heights, then select the local peaks that have periods and λ_z within our range of interest. For this study, these are downward phase progression waves (T and λ_z have the same sign) with periods of 3.15–12 h and λ_z of 5–100 km, respectively. We then set a threshold and select all of the local peaks that are above it. The threshold is set to one-fifth of the global maxima of the 4-D array. If two peaks occur in close proximity and have similar periods and λ_z, these two peaks are marked as one wave and their peak extensions will be combined later. After the selection of qualified local peaks in the 2-D wavelet spectrum, we then scan around those peaks for a contiguously extended region in all four dimensions that fully encapsulates the wave packet. This extended region about a peak is

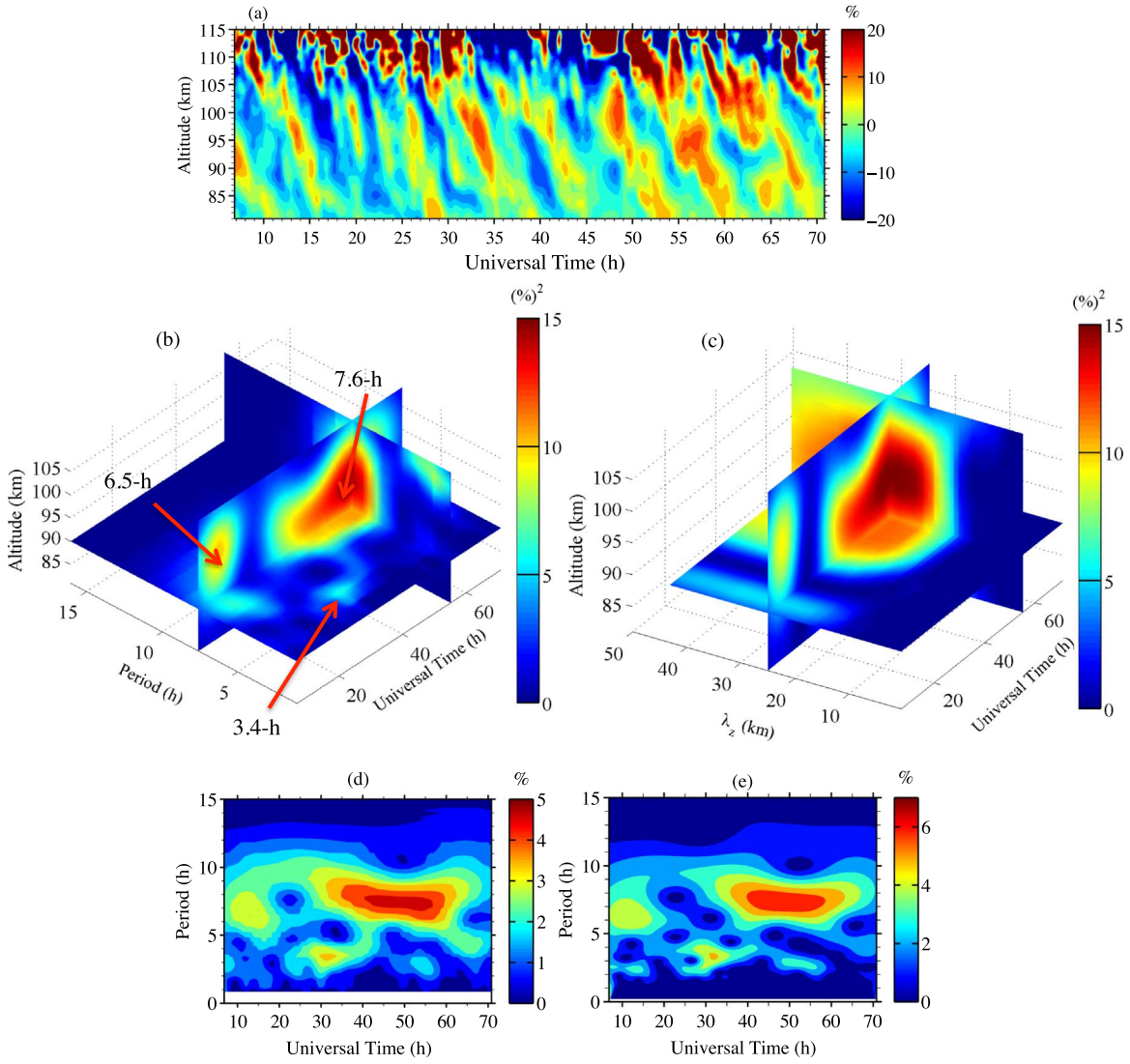

Fig. 3. 3-D illustration of the 2-D Morlet wavelet power spectrum of (a) the relative temperature perturbations during 28–30 June 2014 at (b) λ_z = 25 km and (c) T = 7.6 h. Three slice planes in (b) are at t = 55 UT, z = 90 km, and T = 7.6 h, respectively. Locations of the three major wave packets with periods T ~ 7.6 h, T ~ 6.5 h and T ~ 3.4 h are marked with red arrows. Three slice planes in (c) are at t = 55 UT, z = 90 km, and λ_z = 25 km, respectively. (d) 2-D top view of (b) in the unit of wave amplitude (%), showing how the wave period changes with time at z = 90 km and λ_z = 25 km. (e) 1-D Morlet wavelet amplitude spectrum of the relative temperature perturbations during 28–30 June 2014 at z = 90 km (reproduced from Fig. 4a in Chen et al. (2016a) for easier comparison).

defined as the connected region in which the amplitude of the power spectrum monotonically descends from the peak to where the amplitude either drops below a threshold or begins to increase. In this study, we have used a threshold of 0.5% for the relative temperature perturbations. We confine each search within ± 1/5 of each peak's period so that the connected peak extensions will be quasi-monochromatic in the frequency domain. After each search, the complex wavelet transform coefficients within each peak extension are recorded and this corresponding wave is removed from the next search so that the same wave element will not be recorded twice. The recorded wavelet coefficients of each peak extension are used to reconstruct the 2-D wave matrix using Eq. (35). Note that the whole process of searching, scanning, and reconstruction of each 2-D wave packet is automated. Several wave properties can be inferred from the wavelet coefficients of the peak extensions. First, the total lifespan can be obtained from the earliest appearance of the peak extension at any altitude to the latest appearance at any altitude. Second, the λ_z and vertical phase speed (C_z) can be derived as follows. We derive the vertical profile of the phase line directly from calculating the phase of complex wavelet coefficients within each peak extension. A phase of 2π corresponds to a hot phase in the relative temperature perturbations. This 2π phase line expressed in time is then tracked as a function of altitude, and its derivatives with respect to altitude are determined from linear least square fits within an 8-km window, shifted by 1 km. The inverse of the derivative is C_z, and then C_z multipling period T yields λ_z.

We applied the above automated methods to identify and reconstruct the dominant 2-D wave packets for the ~65 h lidar run from 28 to 30 June 2014. Four wave events were identified, with the wave periods of ~3.4 h, 3.9 h, 6.5 h, and 7.6 h, respectively, and their reconstructed 2-D perturbations are shown in Fig. 4a–d. In order to validate our method, we reconstruct the temperature perturbation field from the sum of these four major wave events in Fig. 4e. The result shows good agreement with the original perturbations field in general, indicating that the reconstructions of the 2-D waves well represent the real atmospheric waves. Each reconstructed 2-D wave is quasi-monochromatic in frequency and, within each wave, all of the phase lines are oriented in a similar direction. The quasi-monochromatic feature of gravity waves is common in the middle atmosphere and has been confirmed many times through observations with lidars and radars in the stratosphere (Gardner et al., 1989; Nastrom and Eaton, 2006; Sato, 1994; Sato et al., 1997; Vaughan and Worthington, 2007; Zink and Vincent, 2001) and with lidars, radars and airglow imagers in the MLT

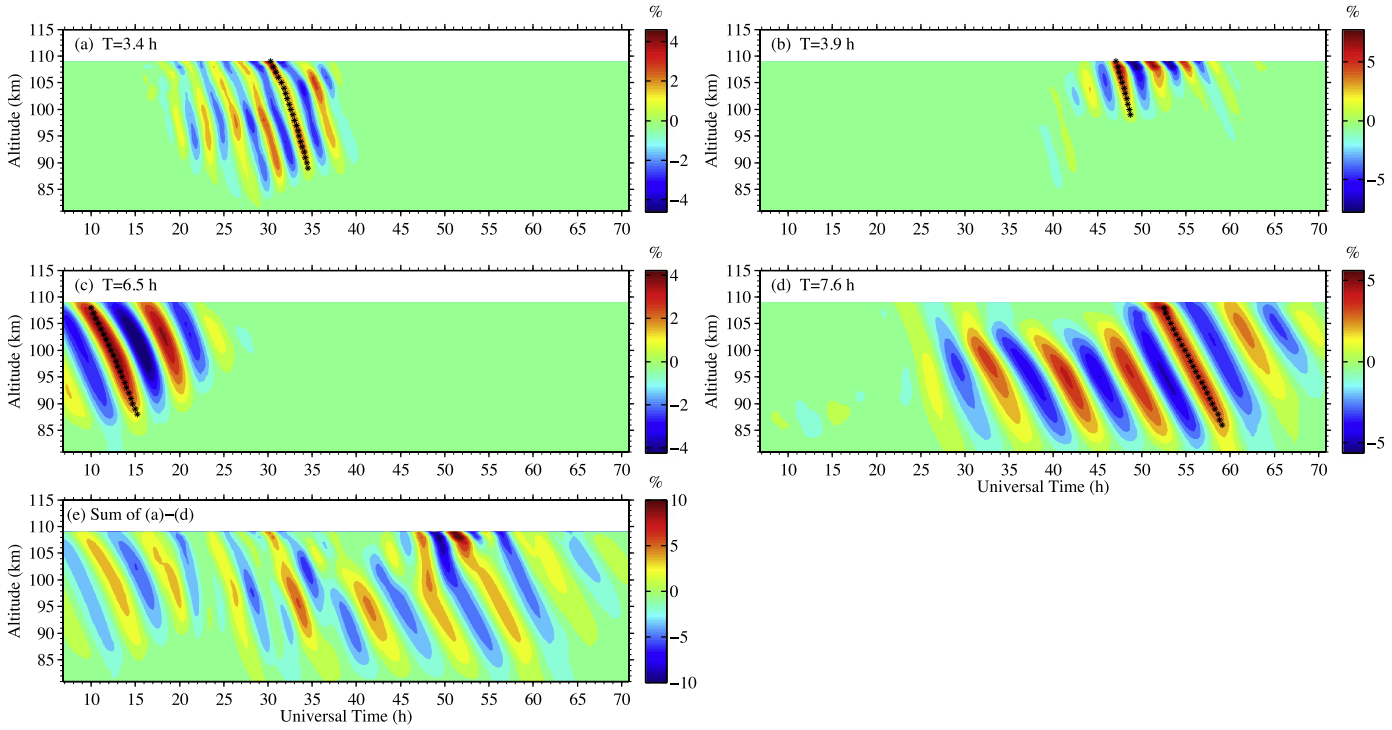

Fig. 4. The 2-D Morlet wavelet reconstruction of four major wave events during 28–30 June 2014 with periods of (a) 3.4 h, (b) 3.9 h, (c) 6.5 h, (d) 7.6 h and (e) the temperature perturbation field reconstructed from combining the above four major wave packets.

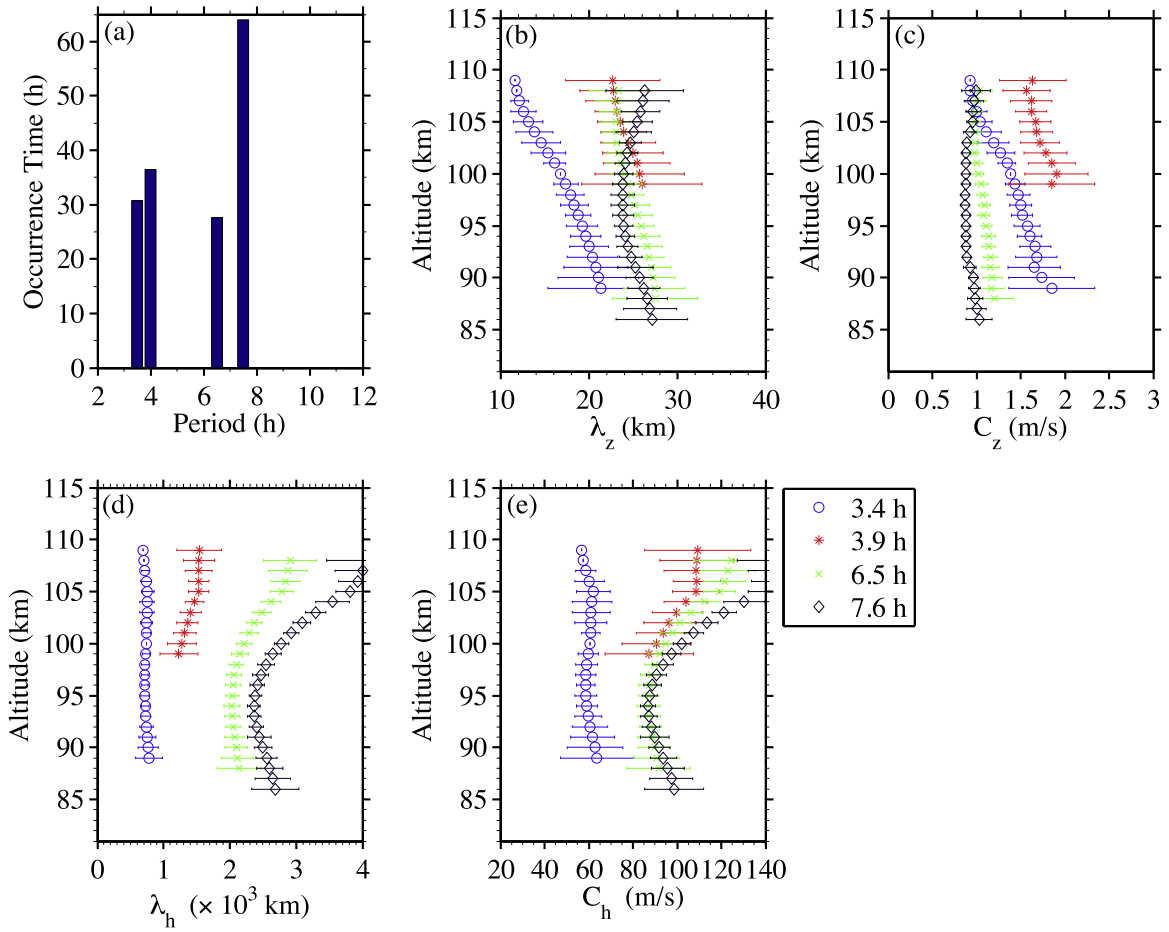

Fig. 5. (a) Life span and vertical profile of (b) vertical wavelength (λ_z), (c) vertical phase speed (C_z), (d) horizontal wavelength (λ_h), and (e) horizontal phase speed (C_h) and their errors (horizontal bars) for each wave event on 28–30 June 2014 derived from the 2-D Morlet wavelet coefficients. Results for each event are denoted in different colors and markers as indicated in the legend. (For interpretation of the references to color in this figure legend, the reader is referred to the web version of this article.)

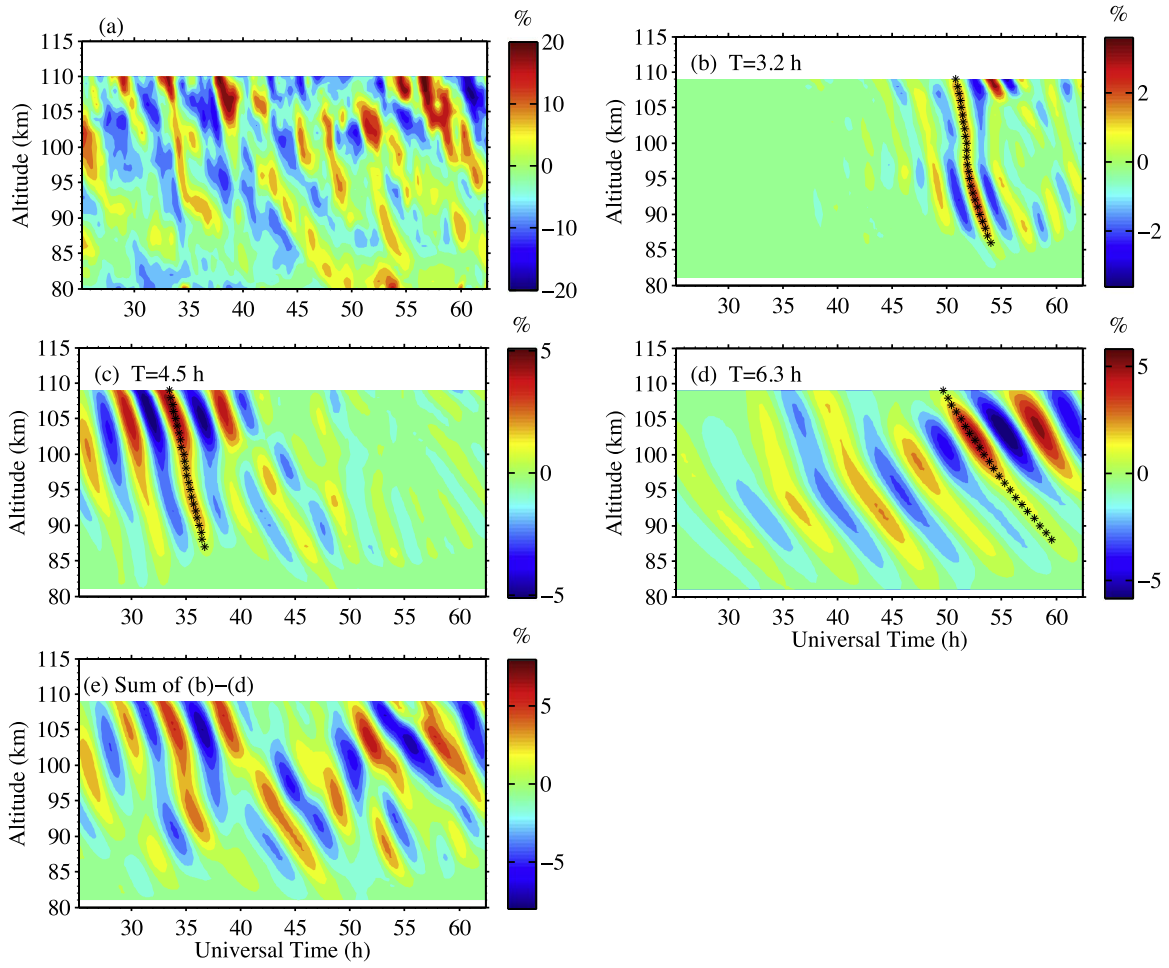

Fig. 6. (a) Original relative temperature perturbations during 23–24 May 2014 and the 2-D wavelet reconstruction of three major wave events with periods of (b) 3.2 h, (c) 4.5 h, (d) 6.3 h, and (e) the temperature perturbation field reconstructed from combining the above three major wave packets.

(Collins et al., 1996; Gardner and Voelz, 1987; Hall et al., 1995; Lu et al., 2015; Nicolls et al., 2010; Taylor et al., 1995; Walterscheid et al., 1999). Therefore, 2-D wavelet methods are suitable for the identification of quasi-monochromatic atmospheric gravity waves in the middle atmosphere. The wave packet nature of these reconstructed waves (i.e., amplitudes varying with time) matches a key character of gravity waves, i.e., they are intermittent. The 2-D wavelet transform can handle this intermittency and can be used to differentiate wave packets.

Compared with the wave events extracted using the 1-D wavelet method in Chen et al. (2016a), the periods of major wave events were found to be nearly identical, considering the period resolution in the wavelet spectral analysis (> 0.5 h at T = 10 h), except that our 2-D program does not discern the 10.6-h wave automatically, as its amplitude is comparable to the noise floor. The amplitude of each 2-D wave is smaller than its counterpart in the 1-D case because the 2-D wavelet is not only selective in the frequency domain, but also the spatial domain. Therefore, the amplitudes shown in the 2-D wavelet spectra represent only a finite λ_z band for the selected period band, unlike those in the 1-D wavelet spectra that contain contributions from all λ_z, even including waves with upward phase progression. The selectivity in the spatial domain is an advantage of the 2-D wavelet and yields a more accurate reconstruction of the 2-D wave packet. The lifespan of each 2-D wave is shown in Fig. 5a. Compared to Chen et al. (2016a), the lifespans of the 3.9 h and 7.6 h waves in this analysis are slightly longer, while lifespans of the 3.4 h and 6.5 h waves are found to be marginally shorter. Due to the 2-D wavelet method's selectivity in the spatial domain, we believe that the 2-D wavelet results are more accurate. Also, due to this selectivity, estimates of the λ_z are less biased than those from the 1-D case. As shown in Fig. 5b, λ_z ranges between 20 and 30 km, except for the 3.4 h wave at upper altitudes. Compared with the results in Chen et al. (2016a), the new results show significant improvement in the estimation of the λ_z for the 6.5-h waves. As shown in Fig. 5c, C_z ranges mostly between 1–2 m/s, comparable to Chen et al. (2016a). The errors of C_z are determined from the 95% confidence levels of the fittings that are used to determine the derivatives of the phase lines. The errors of λ_z are then derived using the error propagation law.

To provide some insight into the nature of these persistent gravity waves, we calculate the horizontal wavelength (λ_h) and horizontal phase speed (C_h) using the gravity wave dispersion relationship for medium frequency waves (see Fritts and Alexander, 2012, 2003 for details). Since the background winds are calm in winter (< 7 m/s) at this height above McMurdo (Baumgaertner et al., 2005), it is reasonable to take ground-based observed frequency ω as the intrinsic frequency $\hat{\omega}$, i.e., assume zero background wind. Then we have

$$k_h^2 = \frac{\omega^2 - f^2}{N^2}\left(m^2 + \frac{1}{4H^2}\right), \tag{38}$$

where k_h is the horizontal wavenumber, m is vertical wavenumber, ω is the observed angular frequency of the wave, f is the Coriolis parameter, $H = R\overline{T}/g$ is the density scale height calculated from the observed mean temperature $\overline{T}$, the gas constant of dry air R, and the gravitational

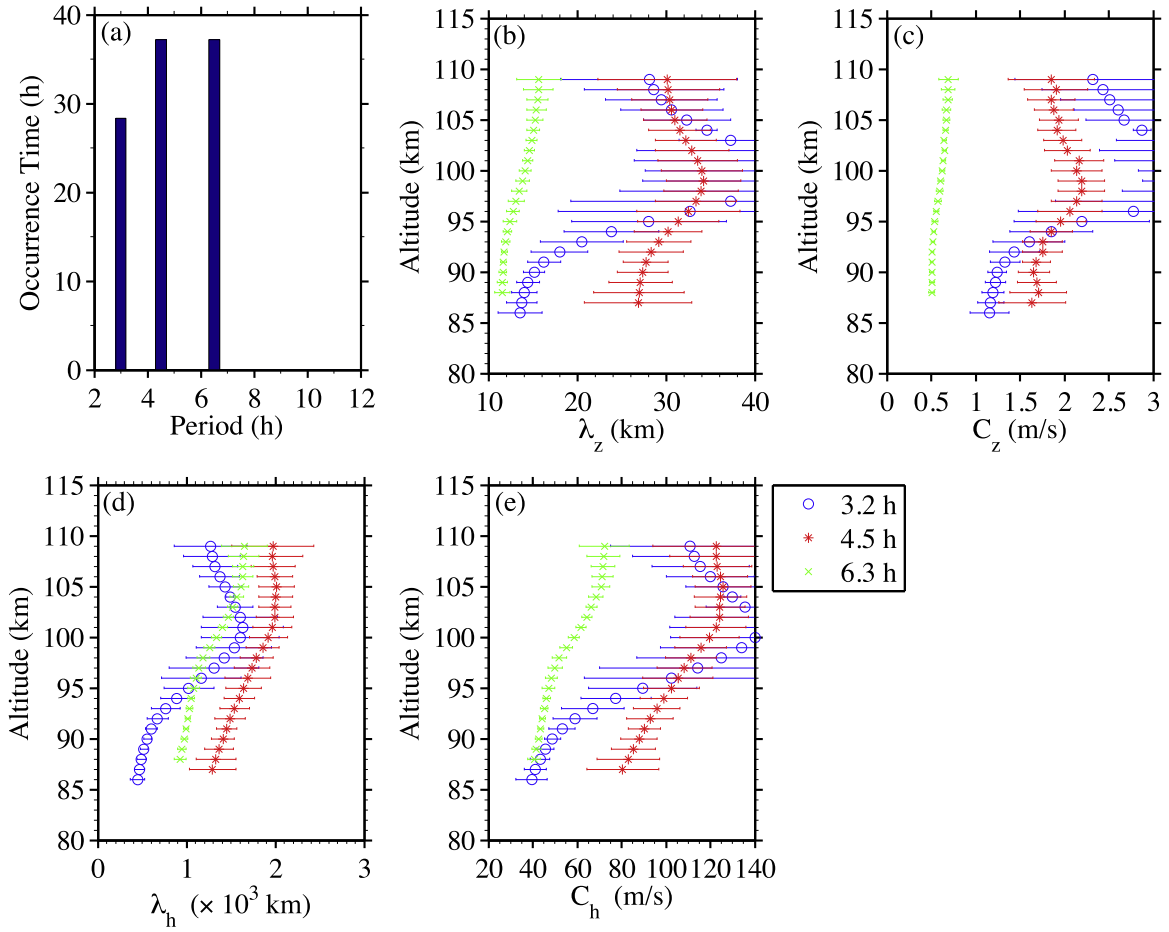

Fig. 7. (a) Life span and vertical profile of (b) λ_z, (c) C_z, (d) λ_h, and (e) C_h and their errors (horizontal bars) for each wave event on 23–24 May 2014 derived from the 2-D Morlet wavelet coefficients. Results for each event are denoted in different colors and markers as indicated in the legend. (For interpretation of the references to color in this figure legend, the reader is referred to the web version of this article.)

acceleration g, and N is the buoyancy frequency computed from $\overline{T}$ as $N = \sqrt{\frac{g}{\overline{T}}\left(\frac{\partial \overline{T}}{\partial z} + \frac{g}{C_p}\right)}$, where C_p is the specific heat capacity at constant pressure. The above calculated λ_h and C_h are shown in Figs. 5d and e. The results show that the λ_h of these waves are ~1000–3000 km, and the C_h are mostly above 60 m/s. The errors shown in the figures are derived from the errors of λ_z and then from the error propagation law.

We also applied the 2-D wavelet analysis and reconstruction to the ~37 h and ~45 h lidar runs of 23–24 May 2014 and 16–18 July 2014 (raw relative temperature perturbations shown in Figs. 6a and 8a, respectively). For both lidar datasets, three wave events were identified automatically and reconstructed using the above methods. Figs. 6b-d show the extracted wave packets of 23–24 May 2014, with periods of ~3.2 h, ~4.5 h and ~6.3 h, respectively, while Fig. 6e shows the reconstruction of the perturbations by combining these major wave events. There are two types of temperature phase lines: two shorter-period (3.2-h and 4.5-h) waves show more vertical phase lines, while the 6.3-h wave shows more oblique phase lines. The derived lifespans, λ_z, C_z, λ_h, and C_h are shown in Fig. 7a–e. The C_z of the 6.3-h wave is ~ 0.5 m/s, indicating that it is more susceptible to atmospheric dissipation than the other two waves, which have shorter periods and faster phase speeds (Vadas, 2007; Vadas and Fritts, 2005). The phase speed of the 3.2-h wave exhibits a large variation with altitude, which could be the result of a more variable background wind condition. Fig. 8b–d show the extracted wave packets of 16–18 July 2014 with periods of ~3.6 h, ~4.8 h, and ~7.8 h, respectively, while Fig. 8e shows the reconstruction from combining these major wave events. As with the May case, this July case also shows two types of temperature phase lines, with the longer period wave exhibiting more oblique phase lines. The derived lifespans, λ_z, C_z, λ_h, and C_h for the July case are shown in Fig. 9a–e. The phase speeds, as with the June case, exhibit fewer variations with altitude. In both the May and July cases, the phase lines of the reconstructed 2-D waves generally show good agreement with the phase lines of the original temperature perturbations. May and July cases show more dynamical wave field structures than the June case. These results indicate that, even in the same winter season, there may be significant month-to-month variability in Antarctic MLT gravity wave activity. Overall, these persistent gravity waves have vertical wavelengths of 20–30 km, vertical phase speeds of 0.5–2 m/s, and horizontal wavelengths of up to several thousands kilometers in the MLT region.

To summarize, the steps of our wave recognition methodology are as follows. First, the 2-D Morlet wavelet forward transform is applied to the 2-D data by computing the wavelet convolution in the frequency domain, as in Eq. (25). The amplitude of the transform is used to calculate the power spectrum, as in Eq. (27). Second, local maxima in the power spectrum are automatically identified and are selected based on their peak heights, periods and λ_z. The contagious extensions of the selected peaks are determined, within which the complex wavelet forward transform coefficients are recorded. Third, the 2-D Morlet wavelet inverse transform is then applied to reconstruct each quasi-monochromatic 2-D wave packet using the recorded transform coefficients, as in Eq. (35). The reconstructed wave packet is for visualization and verification of our method, or can be used to derive wave parameters using other methods (different than our approaches in the final step). Finally, the time span of the contagious extension is taken as the lifespan of the wave packet. The phase of each wave is directly obtained from the phases of the recorded complex wavelet coefficients

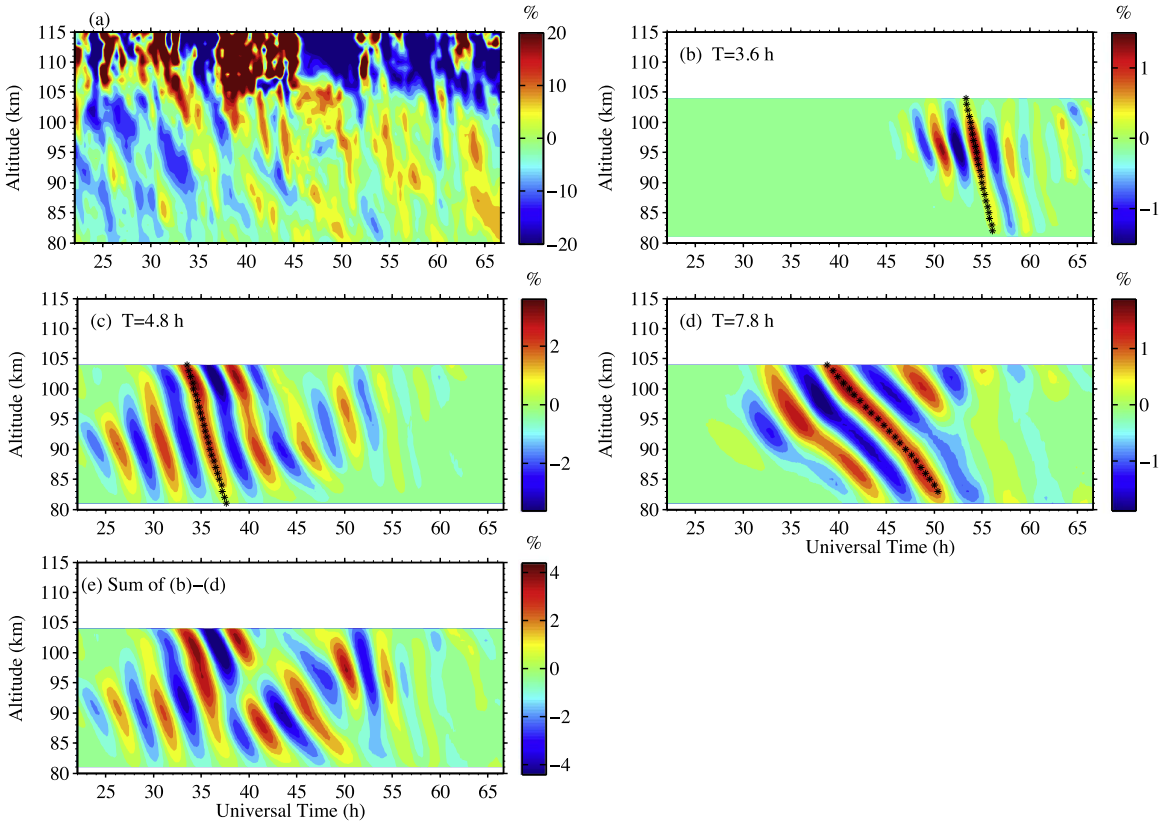

Fig. 8. (a) Original relative temperature perturbations during 16–18 July 2014 and the 2-D wavelet reconstruction of three major wave events with periods of (b) 3.6 h, (c) 4.8 h, (d) 7.8 h, and (e) the temperature perturbation field reconstructed from combining the above three major wave packets.

within that wave's contagious extension. The λ_z and C_z of each wave are derived from the wave phase. The λ_h and C_h are calculated based on the calm wind assumption and the gravity wave dispersion relationship.

6. Discussion

Despite the prosperity of the 2-D wavelet transform and wave recognition methods as demonstrated above, there is still room for improvement. First, it is necessary to investigate the sensitivity of the 2-D wavelet to measurement uncertainties and determine the significance levels for the 2-D wavelet power spectra. For example, when using Fe as a tracer to measure temperature, the errors are largest at the upper and lower boundaries of Fe layers due to the lower signal to noise ratio (SNR). Therefore, measurement uncertainties at upper and lower boundaries can cause false detection of a 2-D wave packet. One solution to this is to weight the raw data by the inverse of their errors prior to the wavelet transform. Nevertheless, effects induced by the measurement uncertainty are not significant since, in the current study, we have selected lidar data with high SNRs. The second issue with extracting atmospheric waves from the raw relative temperature perturbations using the 2-D wavelet transform is that it often favors waves occurring at higher altitudes. The exponential decay of atmospheric density with altitude causes the atmospheric wave amplitude to increase with altitude. This feature makes the extraction of wave packets biased towards the waves at higher altitudes since their amplitudes are larger than those at lower altitudes. This bias can be resolved if the raw data are weighted by the square root of the atmospheric density at each altitude. Finally, the edge effect in the wavelet spectrum (see Torrence and Compo (1998) for details) yields smaller amplitudes at the boundaries of the analysis region. Therefore, the reconstructed wave packets may have smaller amplitudes at the boundaries of the 2-D datasets.

Our method is based on the discretized CWT, which differs from another two common forms of wavelet transforms: the discrete wavelet transform (DWT) and the orthogonal wavelet transform [see Daubechies (1992) for details]. For those who are not familiar with wavelets, they are often confusing, and therefore it is worth to explain the differences. In a discretized CWT, we slide the time series quasi-continuously in small steps with a step size independent of the wavelet scales. However, in a DWT, we slide the time series in large steps (skipping many elements in the series), with a step size dependent on the scale, and do the wavelet transform only where the wavelet envelope almost no longer overlaps the previous wavelet envelopes. Taking the 1-D wavelet as an example, a dilated and translated continuous 1-D wavelet $\psi(s, t) = \frac{1}{\sqrt{s}}\psi(\frac{t'-t}{s})$ will become $\psi(j, n) = \frac{1}{\sqrt{s_0^j}}\psi\left(\frac{t'-nt_0}{s_0^j}\right)$ in a discretized CWT, showing that the translation (at steps $t = nt_0$) has no dependence on the scale s_0^j. However, in a DWT, the above dilated and translated wavelet will become $\psi(j, n) = \frac{1}{\sqrt{s_0^j}}\psi\left(\frac{t'-n\tau_0 s_0^j}{s_0^j}\right)$, where the translation depends on the scale s_0^j and is no longer quasi-continuous. Consequently, higher-frequency wavelets are translated by smaller steps, while lower-frequency wavelets are translated by larger steps in DWT (Daubechies, 1992). Such DWT provides less redundant description of the original time series than a CWT but not the least redundant description. Only for very special choices of ψ, s_0, and τ_0, i.e., when $\psi(j, n)$ are orthogonal and complete, can the redundancy be eliminated entirely. Orthogonal wavelets (e.g., the Harr wavelet and Daubechies wavelet) give the most compact representation of the signal because it decomposes the signal into a minimal number of independent coefficients (Meyers et al., 1993). Due to the extended tails of the Gaussian, it is not possible to construct a truly orthogonal set for the Morlet wavelet. However, for the purpose of determining the precise period (T) or vertical wavelength (λ_z) of

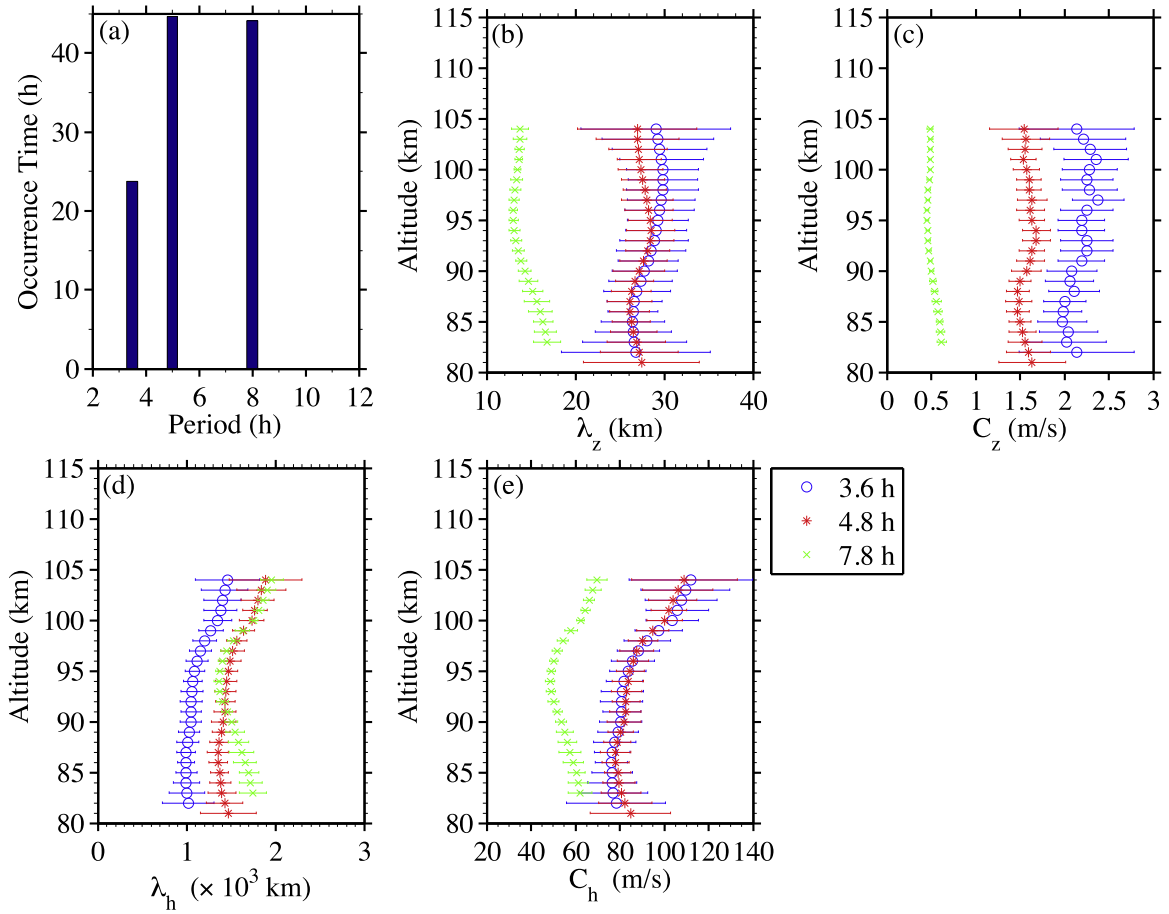

Fig. 9. (a) Life span and vertical profile of (b) λ_z, (c) C_z, (d) λ_h, and (e) C_h and their errors (horizontal bars) for each wave event on 16–18 July 2014 derived from the 2-D Morlet wavelet coefficients. Results for each event are denoted in different colors and markers as indicated in the legend. (For interpretation of the references to color in this figure legend, the reader is referred to the web version of this article.)

a wave, the Morlet wavelet based CWT is advantageous. Firstly, the redundancy of the CWT permits the analysis on a nearly continuous scale grid, which in principle enables a more precise estimation of wave frequency, as opposed to the sparse grid used by the orthogonal wavelets. Secondly, Morlet wavelet's relationship between s, θ and λ_z, T is straightforward and its capability of providing wave phase information allows for the derivation of wave properties such as vertical wavelength and phase speed. Nevertheless, one caveat of the CWT is that it is highly correlated at adjacent times and scales. In the case of two waves with very similar periods and close time spans, it is sometimes not possible to distinguish them and obtain their correct amplitudes using a CWT. After all, Heisenberg uncertainty theorem ($\Delta\omega\cdot\Delta t \geq 1/2$, where $\Delta\omega$ represents the frequency width, and Δt is the time width) limits the joint time and frequency resolutions of wavelets (Mallat, 1999). Therefore, the correctness of wave amplitudes obtained from a CWT should be carefully checked when the input data contain two very similar waves (see Terradellas et al., 2001).

Generally speaking, tropospherically generated inertia-gravity waves (IGWs) are hard to propagate into the MLT region except those that could go through the pipeline in the summer hemisphere (Sato et al., 2009). However, the above estimated C_h of these gravity waves in the MLT (generally around 60–100 m/s) are much faster than those observed in the upper troposphere and stratosphere (typically < 20 m/s) (e.g., Guest et al., 2000; Nastrm and Eaton, 2006; Sato and Yoshiki, 2008; Sato et al., 1997; Shibuya et al., 2015; Vaughan and Worthington, 2007). This suggests that these IGWs could potentially survive the critical level filtering by the strong polar night jet in the winter stratosphere and lower mesosphere over Antarctica. Sato and Yoshiki (2008) demonstrated that the IGWs observed in June were generated by spontaneous geostrophic adjustment of the unbalanced polar night jet located in the stratosphere. This could be the generation mechanism of the IGWs observed at McMurdo during winter seasons, however, the frequently observed summer IGWs (Chu et al., 2011b) cannot be explained by such mechanism, since such a jet is unlikely to exist during the polar summer. Mayr et al. (2004), based on model simulations, suggest that the planetary-scale IGWs in the polar MLT with periods between 9 and 11 h are excited by instabilities that arise in the zonal mean circulation. This could be another possibility of the wave source; however, no clues as to the type of instability were provided.

7. Conclusions and outlook

The wavelet transform, a much newer development in applied mathematics than the well-known Fourier transform, possesses unique features that are attractive to spectral analysis and extraction of waves in the atmosphere and ocean, because many waves are inherently intermittent, with amplitudes, frequencies or wavelengths varying in time and space. However, many conventional wavelet transform codes, such as Torrence and Compo (1998) and MATLAB codes cwtft() and cwtft2(), are biased in favor of low–frequency/large-scale waves. In this paper, we establish the mathematical formalism of modified 1-D and 2-D Morlet wavelet transforms that will eliminate such bias and yield the correct wave amplitudes. We start with a full mathematical description of the 1-D wavelet transform, its inverse transform, and its implementation to demonstrate the construction of an unbiased 1-D wavelet transform based on its physical meaning. To ensure that the powers before and after the wavelet transform

are equivalent, we divide the conventional 1-D wavelet power spectrum by its scale and by a correction factor of π. We then extend the 1-D wavelet transform to two dimensions by rotation, dilation and translation with a full mathematical description, and define our unbiased 2-D wavelet transform with the similar physical basis as in 1-D. Following that, we derive the theoretical relationship between wavelet scale/angle and Fourier period/wavelength. Finally, the methodology of 2-D wavelet reconstruction in the time/space domain is formalized using a delta function.

Based on our modified 2-D Morlet wavelet transform and the reconstruction methods, we developed a wave recognition methodology to automatically extract multiple quasi-monochromatic 2-D wave packets and derive their wave properties. Basically, each major wave packet is recognized through automatically identifying the spectral peaks and determining their contagious extensions in the calculated 2-D wavelet power spectrum. The complex wavelet transform coefficients within each selected peak extension are then used to reconstruct the wave packets for visualization and verification, and to derive wave properties such as the periods, lifespan, λ_z, and C_z. The details of this methodology can be found in Section 5.

The automated wave recognition methodology is then applied to three lidar datasets obtained in the winter of 2014 at McMurdo, Antarctica. The results in the June case are largely similar to those obtained using the 1-D wavelet transform in Chen et al. (2016a), but show significant improvement on the estimates of λ_z and phase speeds. The results in May and July provide additional evidence to confirm our conclusions in Chen et al. (2016a) that these IGWs are persistent and dominant, and exhibit lifetimes of multiple days in winter. If we regard these wave events as a group of waves with periods ranging between 3 and 10 h, then this wave group is perpetual. The three cases in the same winter show different gravity wave features, suggesting the month-to-month variability in gravity wave activity in the Antarctic MLT. Applications of the 2-D Morlet wavelet transform and wave recognition methods to those three cases demonstrate that our methods can faithfully extract wave packets with the desired quasi-monochromatic features and are useful to extract gravity waves that are inherently intermittent.

There are many more potential applications in various science topics and fields for the 2-D Morlet wavelet transform and wave recognition methods that we have developed. For example, such methods could be used to analyze satellite images (e.g., Gong et al., 2015; Zhao et al., 2015), or airglow imager or temperature mapper data to identify 2-D gravity wave packets and estimate their momentum flux (e.g., Bossert et al., 2015; Chen et al., 2016b; Pautet et al., 2016; Yuan et al., 2016). Furthermore, the Morlet wavelet is anisotropic and is therefore suitable to identifying quasi-plane-wave packets. However, by implementing an isotropic wavelet function such as the Halo wavelet (e.g., Wang and Lu, 2010), 2-D wavelet analysis and reconstruction can be used to identify and extract ring structures in concentric gravity waves (see details in Yue et al., 2009) on a horizontal 2-D dataset. This is left as future work.

Acknowledgments

We sincerely acknowledge Dr. Ian Grooms and Dr. Jens Oberheide for valuable discussions on the mathematical formalism of wavelet transforms. We are grateful to Dr. John A. Smith for his English edits, and to Dr. Vladimir Papitashvili for his guidance. We appreciate the staff of the United States Antarctic Program, McMurdo Station, Antarctica New Zealand, and Scott Base for their superb support of the McMurdo lidar campaign. This work was supported by National Science Foundation (NSF) grants PLR-1246405, AGS-1136272, and AGS-1452351. Cao Chen was partially supported by NSF grant AGS-1136272 and a CIRES Graduate Student Research Award during this work. The MATLAB codes and data used in this paper are available upon request.

Appendix A. Derivations of selected equations used in the paper

A.1. Derivation of Eq. (4)

We prove Eq. (4) by showing that the Fourier transforms of the both sides of Eq. (4) are equal. The Fourier transform of the left hand side (LHS) with regard to t is

$$\mathrm{FT[LHS]} = \hat{f}(\omega). \tag{A.1}$$

The Fourier transform of the right hand side (RHS) with regard to t is

$$\begin{aligned}\mathrm{FT[RHS]} &= \frac{1}{C_\psi}\mathrm{FT}\left[\int_0^{+\infty}\int_{-\infty}^{+\infty}\frac{1}{s^2}W_{f\psi}(s,t')\frac{1}{\sqrt{s}}\psi\left(\frac{t-t'}{s}\right)dt'ds\right] = \frac{1}{C_\psi}\mathrm{FT}\left\{\int_0^{+\infty}\int_{-\infty}^{+\infty}\frac{1}{s^2}\left[\frac{1}{\sqrt{s}}f(t)\otimes\psi^*\left(\frac{-t}{s}\right)\right]\frac{1}{\sqrt{s}}\psi\left(\frac{t-t'}{s}\right)dt'ds\right\}\\ &= \frac{1}{C_\psi}\mathrm{FT}\left\{\int_0^{+\infty}\frac{1}{s^2}\left[\frac{1}{\sqrt{s}}f(t)\otimes\psi^*\left(\frac{-t}{s}\right)\right]\otimes\left[\frac{1}{\sqrt{s}}\psi\left(\frac{t}{s}\right)\right]ds\right\} = \frac{1}{C_\psi}\int_0^{+\infty}\frac{1}{s^3}\mathrm{FT}\left[f(t)\otimes\psi^*\left(\frac{-t}{s}\right)\otimes\psi\left(\frac{t}{s}\right)\right]ds\\ &= \frac{1}{C_\psi}\int_0^{+\infty}\frac{1}{s^3}\hat{f}(\omega)\mathrm{FT}\left[\psi^*\left(\frac{-t}{s}\right)\right]\mathrm{FT}\left[\psi\left(\frac{t}{s}\right)\right]ds.\end{aligned} \tag{A.2}$$

Now we rewrite $\mathrm{FT}[\psi(\frac{t}{s})]$ as

$$\mathrm{FT}\left[\psi\left(\frac{t}{s}\right)\right] = \int_{-\infty}^{+\infty}\psi\left(\frac{t}{s}\right)e^{-i\omega t}dt = \int_{-\infty}^{+\infty}\psi\left(\frac{t}{s}\right)e^{-i(s\omega)(\frac{t}{s})}dt = s\int_{-\infty}^{+\infty}\psi\left(\frac{t}{s}\right)e^{-i(s\omega)(\frac{t}{s})}\frac{dt}{s} = s\int_{-\infty}^{+\infty}\psi(t'')e^{-i(s\omega)t''}dt'' = s\hat{\psi}(s\omega), \tag{A.3}$$

and we rewrite $\mathrm{FT}[\psi^*(-\frac{t}{s})]$ as

$$\mathrm{FT}\left[\psi^*\left(-\frac{t}{s}\right)\right] = \int_{-\infty}^{+\infty}\psi^*\left(-\frac{t}{s}\right)e^{-i\omega t}dt = \int_{-\infty}^{+\infty}\psi^*\left(-\frac{t}{s}\right)e^{-i(-s\omega)(-\frac{t}{s})}dt = -s\int_{-\infty}^{+\infty}\psi^*\left(-\frac{t}{s}\right)[e^{-i(s\omega)(-\frac{t}{s})}]^*\frac{dt}{-s} = s\int_{-\infty}^{+\infty}[\psi(t'')e^{-i(s\omega)t''}dt'']^* = s[\hat{\psi}(s\omega)]^*. \tag{A.4}$$

Substituting (A.3) and (A.4) into Eq. (A.2), we obtain

$$\mathrm{FT[RHS]} = \frac{1}{C_\psi}\int_0^{+\infty}\frac{1}{s^3}\hat{f}(\omega)s[\hat{\psi}(s\omega)]^* s\hat{\psi}(s\omega)ds = \frac{\hat{f}(\omega)}{C_\psi}\int_0^{+\infty}|\hat{\psi}(s\omega)|^2\frac{ds}{s}. \tag{A.5}$$

Eq. (A.5) reduces to (A.1), if $C_\psi = \int_0^{+\infty}|\hat{\psi}(s\omega)|^2\frac{ds}{s} < +\infty$. We only need to prove that this condition is essentially the same as Eq. (3) for any real wavelet function $\psi(t)$. Rewriting the equation, we have

$$C_\psi = \int_0^{+\infty}|\hat{\psi}(s\omega)|^2\frac{\omega ds}{s\omega} = \begin{cases}\int_0^{+\infty}|\hat{\psi}(\chi)|^2\frac{d\chi}{\chi}, & \text{when } \omega \geq 0\\ \int_0^{-\infty}|\hat{\psi}(\chi)|^2\frac{d\chi}{\chi}, & \text{when } \omega < 0\end{cases} = \begin{cases}\int_0^{+\infty}|\hat{\psi}(\chi)|^2\frac{d\chi}{\chi}, & \text{when } \omega \geq 0\\ \int_0^{+\infty}|\hat{\psi}(-\gamma)|^2\frac{d\gamma}{\gamma}, & \text{when } \omega < 0\end{cases}. \tag{A.6}$$

Since the wavelet function $\psi(t)$ is real, we have $|\hat{\psi}(\omega)|^2 = |\hat{\psi}(-\omega)|^2$. Then (A.6) reduces to Eq. (3),

$$C_\psi = \int_0^{+\infty}\frac{|\hat{\psi}(\omega)|^2}{\omega}d\omega.$$

Under condition $C_\psi = \int_0^{+\infty}\frac{|\hat{\psi}(\omega)|^2}{\omega}d\omega < \infty$, FT[LHS] = FT[RHS], and therefore we have proved Eq. (4).

A.2. Derivation of Eq. (8)

We first rewrite the RHS of Eq. (8) using the Parseval's theorem,

$$\begin{aligned}\mathrm{RHS} &= \frac{1}{C_\psi}\int_0^{+\infty}\int_{-\infty}^{+\infty}|W_{f\psi}(s,t)|^2dt\frac{ds}{s^2} = \frac{1}{2\pi C_\psi}\int_0^{+\infty}\int_{-\infty}^{+\infty}|\hat{W}_{f\psi}(s,\omega)|^2d\omega\frac{ds}{s^2} = \frac{1}{2\pi C_\psi}\int_0^{+\infty}\int_{-\infty}^{+\infty}s|\hat{f}(\omega)|^2|\hat{\psi}(s\omega)|^2\,d\omega\frac{ds}{s^2}\\ &= \frac{1}{2\pi C_\psi}\int_{-\infty}^{+\infty}|\hat{f}(\omega)|^2\left[\int_0^{+\infty}|\hat{\psi}(s\omega)|^2\frac{ds}{s}\right]d\omega.\end{aligned} \tag{A.7}$$

For a real wavelet function $\psi(t)$, we have proven that $C_\psi = \int_0^{+\infty}|\hat{\psi}(s\omega)|^2\frac{ds}{s} < +\infty$. Therefore,RHS $= \frac{1}{2\pi}\int_{-\infty}^{+\infty}|\hat{f}(\omega)|^2d\omega = \int_{-\infty}^{+\infty}|f(t)|^2dt$ = LHS.
In the case of a complex wavelet function $\psi(t)$ and a real $f(t)$, we have

$$\mathrm{RHS} = \frac{1}{2\pi C_\psi}\left\{\int_0^{+\infty}|\hat{f}(\omega)|^2\left[\int_0^{+\infty}|\hat{\psi}(s\omega)|^2\frac{ds}{s}\right]d\omega\right\} \tag{A.8}$$

$$+\frac{1}{2\pi C_\psi}\left\{\int_{-\infty}^{0}|\hat{f}(\omega)|^2\left[\int_0^{+\infty}|\hat{\psi}(s\omega)|^2\frac{ds}{s}\right]d\omega\right\} \tag{A.9}$$

Since $\omega > 0$ in (A.8), by substituting $\chi = s\omega \geq 0$, we can rewrite (A.8) as

$$\frac{1}{2\pi C_\psi}\left\{\int_0^{+\infty}|\hat{f}(\omega)|^2\left[\int_0^{+\infty}|\hat{\psi}(\chi)|^2\frac{d\chi}{\chi}\right]d\omega\right\}. \tag{A.10}$$

However, $\omega < 0$ in (A.9), by substituting $\gamma = -s\omega \geq 0$ and $\zeta = -\omega$, we can rewrite (A.9) as

$$\frac{1}{2\pi C_\psi}\left\{\int_0^{+\infty}|\hat{f}(-\zeta)|^2\left[\int_0^{+\infty}|\hat{\psi}(-\gamma)|^2\frac{d\gamma}{\gamma}\right]d\zeta\right\}. \tag{A.11}$$

Utilizing $|\hat{f}(\omega)|^2 = |\hat{f}(-\omega)|^2$ for real $f(t)$, we have

$$\mathrm{RHS} = \frac{1}{2\pi C_\psi}\left[\int_0^{+\infty}|\hat{f}(\omega)|^2d\omega\right]\left[\int_0^{+\infty}|\hat{\psi}(\chi)|^2\frac{d\chi}{\chi} + \int_0^{+\infty}|\hat{\psi}(-\gamma)|^2\frac{d\gamma}{\gamma}\right] = \frac{1}{2\pi C_\psi}\left[\int_0^{+\infty}|\hat{f}(\omega)|^2d\omega\right]\left[\int_0^{+\infty}\frac{|\hat{\psi}(\chi)|^2 + |\hat{\psi}(-\chi)|^2}{\chi}d\chi\right]. \tag{A.12}$$

Substituting the definition of $C_\psi = \int_0^{+\infty}\frac{|\hat{\psi}(\chi)|^2 + |\hat{\psi}(-\chi)|^2}{2\chi}d\chi$ from Eqs. (6) to (A.12) yields

$$\mathrm{RHS} = \frac{1}{2\pi}\left[2\cdot\int_0^{+\infty}|\hat{f}(\omega)|^2d\omega\right] = \frac{1}{2\pi}\left[\int_{-\infty}^{+\infty}|\hat{f}(\omega)|^2d\omega\right] = \int_{-\infty}^{+\infty}|f(t)|^2dt = \mathrm{LHS}. \tag{A.13}$$

A.3. Relationship between wavelet scale and Fourier period

Substitute a cosine function $f(t) = A_1cos(\omega_1 t + \varphi_1)$ with Fourier transform of

$$\hat{f}(\omega) = \pi A_1[\delta(\omega - \omega_1)e^{i\varphi_1} + \delta(\omega + \omega_1)e^{-i\varphi_1}] \tag{A.14}$$

into Eq. (11).

$$\begin{aligned}P_f(s,t) &= \frac{1}{C_\psi'^2}\left|\frac{1}{\sqrt{2\pi}}\int_{-\infty}^{+\infty}\hat{f}(\omega)e^{\frac{-(s\omega-\omega_0)^2}{2}}e^{i\omega t}d\omega\right|^2 = \frac{1}{C_\psi'^2}\left|\frac{1}{\sqrt{2\pi}}\int_{-\infty}^{+\infty}\pi A_1[\delta(\omega-\omega_1)e^{i\varphi_1} + \delta(\omega+\omega_1)e^{-i\varphi_1}]e^{\frac{-(s\omega-\omega_0)^2}{2}}e^{i\omega t}d\omega\right|^2\\ &= \frac{\pi A_1^2}{2C_\psi'^2}\left|\left[e^{\frac{-(s\omega_1-\omega_0)^2}{2}}e^{i(\omega_1 t+\varphi_1)} + e^{\frac{-(s\omega_1+\omega_0)^2}{2}}e^{-i(\omega_1 t+\varphi_1)}\right]\right|^2\end{aligned} \tag{A.15}$$

Since $s > 0$, $\omega_0 = 6$ and we can assume $\omega_1 > 0$ without losing generality, the second term on RHS can be neglected ($e^{\frac{-(s\omega_1+\omega_0)^2}{2}} < e^{-\frac{\omega_0^2}{2}} \sim 1.5\times10^{-8}$).

$$P_f(s,t) = \frac{\pi A_1^2}{2C_\psi'^2} e^{-(s\omega_1-\omega_0)^2} \tag{A.16}$$

To find the maximum value of $P_f(s,t)$, we set the derivative of (A.16) with respect to s to zero and obtain

$$\frac{\partial P_f(s,t)}{\partial s} = -\frac{\pi A_1^2}{C_\psi'^2}(s\omega_1-\omega_0)\omega_1 e^{-(s\omega_1-\omega_0)^2} = 0 \tag{A.17}$$

The only solution is $s = \omega_0/\omega_1 = \omega_0 T_1/2\pi$, where T_1 is the Fourier period. The maximum value $P_f(s,t)$ is then equal to $\pi A_1^2/2C_\psi'^2$. By setting this maxima equal to the signal's mean power ($A_1^2/2$), we obtain $C_\psi' = \sqrt{\pi}$.

A.4. Derivation of Eq. (20)

Similar to the 1-D case, we prove Eq. (20) by showing that the Fourier transforms of the both sides of the Eq. (20) are equal. The Fourier transform of the LHS with regard to $\vec{t}$ is

$$\mathrm{FT[LHS]} = \hat{f}(\vec{\omega}). \tag{A.18}$$

The Fourier transform of the RHS with regard to $\vec{t}$ is

$$\begin{aligned}\mathrm{FT[RHS]} &= \frac{1}{C_\psi}\mathrm{FT}\left[\int_0^{2\pi}\int_0^{+\infty}\int_{-\infty}^{+\infty}\int_{-\infty}^{+\infty}\frac{1}{s^3}W_{f\psi}(s,\theta,\vec{t}\,')\frac{1}{s}\psi\left(\Omega_\theta^{-1}\frac{\vec{t}-\vec{t}\,'}{s}\right)d\vec{t}\,'dsd\theta\right]\\ &= \frac{1}{C_\psi}\mathrm{FT}\left\{\int_0^{2\pi}\int_0^{+\infty}\frac{1}{s^3}\left[f(\vec{t})\otimes\frac{1}{s}\psi^*\left(\frac{-\Omega_\theta^{-1}\vec{t}}{s}\right)\right]\otimes\frac{1}{s}\psi\left(\frac{\Omega_\theta^{-1}\vec{t}}{s}\right)dsd\theta\right\} = \frac{1}{C_\psi}\int_0^{2\pi}\int_0^{+\infty}\frac{1}{s^3}\hat{f}(\vec{\omega})\mathrm{FT}\left[\frac{1}{s}\psi^*\left(\frac{-\Omega_\theta^{-1}\vec{t}}{s}\right)\right]\mathrm{FT}\left[\frac{1}{s}\psi\left(\frac{\Omega_\theta^{-1}\vec{t}}{s}\right)\right]dsd\theta.\end{aligned} \tag{A.19}$$

Now we rewrite $\mathrm{FT}\left[\frac{1}{s}\psi^*\left(\frac{-\Omega_\theta^{-1}\vec{t}}{s}\right)\right]$ as

$$\mathrm{FT}\left[\frac{1}{s}\psi^*\left(\frac{-\Omega_\theta^{-1}\vec{t}}{s}\right)\right] = \int_{-\infty}^{+\infty}\int_{-\infty}^{+\infty}\frac{1}{s}\psi^*\left(-\frac{t\cos\theta+z\sin\theta}{s},-\frac{-t\sin\theta+z\cos\theta}{s}\right)e^{-i\omega t}e^{-imz}dtdz. \tag{A.20}$$

We change the variables (t, z) to a new set of variables (u, v),

$$\begin{aligned}u &= -\frac{t\cos\theta+z\sin\theta}{s},\\ v &= \frac{t\sin\theta-z\cos\theta}{s}.\end{aligned} \tag{A.21}$$

Then Eq. (A.20) is rewritten as

$$\begin{aligned}\mathrm{FT}\left[\frac{1}{s}\psi^*\left(\frac{-\Omega_\theta^{-1}\vec{t}}{s}\right)\right] &= \int_{-\infty}^{+\infty}\int_{-\infty}^{+\infty}\frac{1}{s}\psi^*(u,v)e^{-is\omega(v\sin\theta-u\cos\theta)}e^{ism(u\sin\theta+v\cos\theta)}\left|\frac{\partial(t,z)}{\partial(u,v)}\right|dudv = \int_{-\infty}^{+\infty}\int_{-\infty}^{+\infty}\frac{1}{s}\psi^*(u,v)e^{is(\omega\cos\theta+m\sin\theta)u}e^{-is(\omega\sin\theta-m\cos\theta)v}s^2dudv\\ &= \int_{-\infty}^{+\infty}\int_{-\infty}^{+\infty}s\psi^*(u,v)e^{is(\omega\cos\theta+m\sin\theta)u}e^{-is(\omega\sin\theta-m\cos\theta)v}dudv = s\left[\int_{-\infty}^{+\infty}\int_{-\infty}^{+\infty}\psi(u,v)e^{-is(\omega\cos\theta+m\sin\theta)u}e^{-is(-\omega\sin\theta+m\cos\theta)v}dudv\right]^*\\ &= s[\hat{\psi}(s\omega\cos\theta+sm\sin\theta,-s\omega\sin\theta+sm\cos\theta)]^* = s[\hat{\psi}(s\Omega_\theta^{-1}\vec{\omega})]^*,\end{aligned} \tag{A.22}$$

where $\left|\frac{\partial(t,z)}{\partial(u,v)}\right|$ is the determinant of the Jacobian Matrix. Similarly, we rewrite $\mathrm{FT}\left[\frac{1}{s}\psi\left(\frac{\Omega_\theta^{-1}\vec{t}}{s}\right)\right]$ as,

$$\mathrm{FT}\left[\frac{1}{s}\psi\left(\frac{\Omega_\theta^{-1}\vec{t}}{s}\right)\right] = s\hat{\psi}(s\Omega_\theta^{-1}\vec{\omega}). \tag{A.23}$$

Substituting (A.22) and (A.23) into Eq. (A.19), we obtain

$$\mathrm{FT[RHS]} = \frac{1}{C_\psi}\int_0^{2\pi}\int_0^{+\infty}\frac{1}{s^3}\hat{f}(\vec{\omega})s^2|\hat{\psi}(s\Omega_\theta^{-1}\vec{\omega})|^2dsd\theta = \frac{1}{C_\psi}\int_0^{2\pi}\int_0^{+\infty}\hat{f}(\vec{\omega})|\hat{\psi}(s\Omega_\theta^{-1}\vec{\omega})|^2\frac{ds}{s}d\theta. \tag{A.24}$$

Eq. (A.24) reduces to (A.18), if $C_\psi = \int_0^{2\pi}\int_0^{+\infty}|\hat{\psi}(s\Omega_\theta^{-1}\vec{\omega})|^2\frac{ds}{s}d\theta < +\infty$. We only need to prove that this condition is essentially the same as Eq. (19) for any 2-D wavelet function $\psi(\vec{t})$. Rewriting the equation, by changing the variables (s, θ) to a new set of variables (x, y),

$$x = s(\omega\cos\theta + m\sin\theta),\ y = s(-\omega\sin\theta + m\cos\theta). \tag{A.25}$$

Or equivalently, the transform is

$$s = \sqrt{\frac{x^2+y^2}{\omega^2+m^2}},\ \theta = arctan(\frac{m}{\omega}) - arctan(\frac{y}{x}). \tag{A.26}$$

Changing the variables, we obtain

$$C_\psi = \int_0^{2\pi}\int_0^{+\infty}|\hat{\psi}(s\Omega_\theta^{-1}\vec{\omega})|^2\frac{ds}{s}d\theta = \int_{-\infty}^{+\infty}\int_{-\infty}^{+\infty}|\hat{\psi}(x,y)|^2\frac{1}{s}\left|\frac{\partial(s,\theta)}{\partial(x,y)}\right|dxdy = \int_{-\infty}^{+\infty}\int_{-\infty}^{+\infty}|\hat{\psi}(x,y)|^2\frac{1}{s}\frac{1}{s|\omega|^2}dxdy = \int_{-\infty}^{+\infty}\int_{-\infty}^{+\infty}\frac{|\hat{\psi}(x,y)|^2}{x^2+y^2}dxdy. \tag{A.27}$$

Under condition $C_\psi = \int_{-\infty}^{+\infty}\int_{-\infty}^{+\infty}\frac{|\hat{\psi}(x,y)|^2}{x^2+y^2}dxdy < +\infty$, FT[LHS] = FT[RHS], and therefore we have proved Eq. (20).

A.5. Derivation of Eq. (21)

The Fourier transform of the LHS of Eq. (21) with regard to $\vec{t}$ is $\hat{f}(\vec{\omega})$. The Fourier transform of the RHS with regard to $\vec{t}$ is

$$\begin{aligned}
\mathrm{FT[RHS]} &= \frac{1}{C_\psi}\mathrm{FT}\left[\int_0^\pi\int_0^{+\infty}\int_{-\infty}^{+\infty}\int_{-\infty}^{+\infty}\frac{1}{s^3}\Re\left[W_{f\psi}(s,\theta,\vec{t}\,')\frac{1}{s}\psi\left(\Omega_\theta^{-1}\frac{\vec{t}-\vec{t}\,'}{s}\right)\right]d\vec{t}\,'dsd\theta\right]\\
&= \frac{1}{2C_\psi}\mathrm{FT}\left\{\int_0^\pi\int_0^{+\infty}\frac{1}{s^3}\left[f(\vec{t})\otimes\frac{1}{s}\psi^*\left(\frac{-\Omega_\theta^{-1}\vec{t}}{s}\right)\otimes\frac{1}{s}\psi\left(\frac{\Omega_\theta^{-1}\vec{t}}{s}\right)+f(\vec{t})\otimes\frac{1}{s}\psi\left(\frac{-\Omega_\theta^{-1}\vec{t}}{s}\right)\otimes\frac{1}{s}\psi^*\left(\frac{\Omega_\theta^{-1}\vec{t}}{s}\right)\right]dsd\theta\right\}\\
&= \frac{1}{2C_\psi}\int_0^\pi\int_0^{+\infty}\frac{1}{s^3}\left\{\hat{f}(\vec{\omega})\mathrm{FT}\left[\frac{1}{s}\psi^*\left(\frac{-\Omega_\theta^{-1}\vec{t}}{s}\right)\right]\mathrm{FT}\left[\frac{1}{s}\psi\left(\frac{\Omega_\theta^{-1}\vec{t}}{s}\right)\right]+\hat{f}(\vec{\omega})\mathrm{FT}\left[\frac{1}{s}\psi\left(\frac{-\Omega_\theta^{-1}\vec{t}}{s}\right)\right]\mathrm{FT}\left[\frac{1}{s}\psi^*\left(\frac{\Omega_\theta^{-1}\vec{t}}{s}\right)\right]\right\}dsd\theta\\
&= \frac{1}{2C_\psi}\int_0^\pi\int_0^{+\infty}\frac{1}{s^3}\hat{f}(\vec{\omega})[s\hat{\psi}^*(s\Omega_\theta^{-1}\vec{\omega})][s\hat{\psi}(s\Omega_\theta^{-1}\vec{\omega})]+\hat{f}(\vec{\omega})[s\hat{\psi}(-s\Omega_\theta^{-1}\vec{\omega})][s\hat{\psi}^*(-s\Omega_\theta^{-1}\vec{\omega})]dsd\theta\\
&= \frac{\hat{f}(\vec{\omega})}{C_\psi}\int_0^\pi\int_0^{+\infty}[|\hat{\psi}(s\Omega_\theta^{-1}\vec{\omega})|^2+|\hat{\psi}(-s\Omega_\theta^{-1}\vec{\omega})|^2]\frac{ds}{s}d\theta = \frac{\hat{f}(\vec{\omega})}{2C_\psi}\left[\int_0^\pi\int_0^{+\infty}|\hat{\psi}(s\Omega_\theta^{-1}\vec{\omega})|^2\frac{ds}{s}d\theta+\int_\pi^{2\pi}\int_0^{+\infty}|\hat{\psi}(s\Omega_{\theta'}^{-1}\vec{\omega})|^2\frac{ds}{s}d\theta'\right]\\
&= \frac{\hat{f}(\vec{\omega})}{2C_\psi}\int_0^{2\pi}\int_0^{+\infty}|\hat{\psi}(s\Omega_\theta^{-1}\vec{\omega})|^2\frac{ds}{s}d\theta = \frac{\hat{f}(\vec{\omega})}{2C_\psi}\int_{-\infty}^{+\infty}\int_{-\infty}^{+\infty}\frac{|\hat{\psi}(x,y)|^2}{x^2+y^2}dxdy.
\end{aligned} \tag{A.28}$$

Under condition $C_\psi = \int_{-\infty}^{+\infty}\int_{-\infty}^{+\infty}\frac{|\hat{\psi}(x,y)|^2}{2(x^2+y^2)}dxdy < +\infty$, FT[LHS] = FT[RHS], and therefore we have proved Eq. (21).

A.6. Derivation of Eq. (23)

Similar to the 1-D case, we rewrite the RHS of Eq. (23) using the Parseval's theorem in two dimensions,

$$\begin{aligned}
\mathrm{RHS} &= \frac{1}{C_\psi}\int_0^{2\pi}\int_0^{+\infty}\int_{-\infty}^{+\infty}\int_{-\infty}^{+\infty}|W_{f\psi}(s,\theta,\vec{t})|^2\frac{1}{s^2}d\vec{t}\frac{ds}{s}d\theta = \frac{1}{C_\psi}\int_0^{2\pi}\int_0^{+\infty}\int_{-\infty}^{+\infty}\int_{-\infty}^{+\infty}|\hat{W}_{f\psi}(s,\theta,\vec{\omega})|^2\frac{1}{s^2}d\vec{\omega}\frac{ds}{s}d\theta\\
&= \frac{1}{C_\psi}\int_0^{2\pi}\int_0^{+\infty}\int_{-\infty}^{+\infty}\int_{-\infty}^{+\infty}|\hat{f}(\vec{\omega})s\hat{\psi}^*(s\Omega_\theta^{-1}\vec{\omega})|^2\frac{1}{s^2}d\vec{\omega}\frac{ds}{s}d\theta = \int_0^{2\pi}\int_0^{+\infty}\int_{-\infty}^{+\infty}\int_{-\infty}^{+\infty}|\hat{f}(\vec{\omega})|^2|\hat{\psi}(s\Omega_\theta^{-1}\vec{\omega})|^2d\vec{\omega}\frac{ds}{s}d\theta\\
&= \int_{-\infty}^{+\infty}\int_{-\infty}^{+\infty}|\hat{f}(\vec{\omega})|^2\left[\int_0^{2\pi}\int_0^{+\infty}\frac{|\hat{\psi}(s\Omega_\theta^{-1}\vec{\omega})|^2}{C_\psi}\frac{ds}{s}d\theta\right]d\vec{\omega} = \int_{-\infty}^{+\infty}\int_{-\infty}^{+\infty}|f(\vec{t})|^2d\vec{t} = \mathrm{LHS}.
\end{aligned} \tag{A.29}$$

A.7. Relationship between the 2-D wavelet angles and scales and the Fourier frequencies and vertical wavenumbers

Substitute a cosine function $f(\vec{t}) = A_1 cos(\omega_1 t + m_1 z)$ with Fourier transform of

$$\hat{f}(\vec{\omega}) = 2\pi^2 A_1[\delta(\omega-\omega_1)\delta(m-m_1)+\delta(\omega+\omega_1)\delta(m+m_1)] \tag{A.30}$$

into Eq. (24), we obtain

$$\begin{aligned}
P_f(s,\theta,\vec{t}) &= \frac{1}{C_\psi'^2}\left|\frac{1}{2\pi}\int_{-\infty}^{+\infty}\int_{-\infty}^{+\infty}f(\vec{\omega})e^{\frac{-|s\vec{\omega}-\vec{\omega}_0'(\theta)|^2}{2}}e^{i\vec{\omega}\cdot\vec{t}}d\vec{\omega}\right|^2\\
&= \frac{1}{C_\psi'^2}\left|\frac{1}{2\pi}\int_{-\infty}^{+\infty}\int_{-\infty}^{+\infty}2\pi^2A_1[\delta(\omega-\omega_1)\delta(m-m_1)+\delta(\omega+\omega_1)\delta(m+m_1)]e^{\frac{-|s\vec{\omega}-\vec{\omega}_0'(\theta)|^2}{2}}e^{i\vec{\omega}\cdot\vec{t}}d\vec{\omega}\right|^2 \approx \frac{\pi^2A_1^2}{C_\psi'^2}e^{-[(s\omega_1-\omega_0cos\theta)^2+(sm_1-\omega_0sin\theta)^2]}.
\end{aligned} \tag{A.31}$$

$P_f(s,\theta,\vec{t})$ reaches its maximum value $\pi^2A_1^2/C_\psi'^2$ at $s=\sqrt{\omega_0^2/(m_1^2+\omega_1^2)}$ and $\theta = tan^{-1}(m_1/\omega_1)$. By setting this maxima equal to the signal's mean power $(A_1^2/2)$, we obtain $C_\psi' = \sqrt{2}\pi$.

References

Alexander, M.J., Dunkerton, T.J., 1999. A spectral parameterization of mean-flow forcing due to breaking gravity waves. J. Atmos. Sci. 56, 4167–4182. http://dx.doi.org/10.1175/1520-0469(1999)056 < 4167:ASPOMF > 2.0.CO;2.

Baumgaertner, A.J.G., McDonald, A.J., Fraser, G.J., Plank, G.E., 2005. Long-term observations of mean winds and tides in the upper mesosphere and lower thermosphere above Scott Base, Antarctica. J. Atmos. Sol. Terr. Phys. 67, 1480–1496. http://dx.doi.org/10.1016/j.jastp.2005.07.018.

Bossert, K., Fritts, D.C., Pautet, P.-D., Williams, B.P., Taylor, M.J., Kaifler, B., Dörnbrack, A., Reid, I.M., Murphy, D.J., Spargo, A.J., MacKinnon, A.D., 2015. Momentum flux estimates accompanying multiscale gravity waves over Mount Cook, New Zealand, on 13 July 2014 during the DEEPWAVE campaign. J. Geophys. Res. Atmos. 120, 9323–9337. http://dx.doi.org/10.1002/2015JD023197.

Chen, C., Chu, X., McDonald, A.J., Vadas, S.L., Yu, Z., Fong, W., Lu, X., 2013. Inertia-gravity waves in Antarctica: a case study using simultaneous lidar and radar measurements at McMurdo/Scott Base (77.8 °S, 166.7 °E). J. Geophys. Res. Atmos. 118, 2794–2808. http://dx.doi.org/10.1002/jgrd.50318.

Chen, C., Chu, X., Zhao, J., Roberts, B.R., Yu, Z., Fong, W., Lu, X., Smith, J.A., 2016a. Lidar observations of persistent gravity waves with periods of 3–10 h in the Antarctic middle and

upper atmosphere at McMurdo (77.83 °S, 166.67 °E). J. Geophys. Res. Sp. Phys. 121, 1483–1502. http://dx.doi.org/10.1002/2015JA022127.
Chen, C., Chu, X., Fong, W., Lu, X., McDonald, A.J., Pautet, D., Taylor, M., 2016b. Antarctic Wave Dynamics Mystery Discovered by Lidar, Radar and Imager, In: Gross, B., Moshary, F., Arend, M. (Eds.), Proceedings of the 27th International Laser Radar Conference. New York, NY, p. 13004. doi:10.1051/epjconf/201611913004.
Chu, X., Pan, W., Papen, G.C., Gardner, C.S., Gelbwachs, J.A., 2002. Fe Boltzmann temperature Lidar: design, error analysis, and initial results at the North and South Poles. Appl. Opt. 41, 4400–4410. http://dx.doi.org/10.1364/AO.41.004400.
Chu, X., Yu, Z., Gardner, C.S., Chen, C., Fong, W., 2011a. Lidar observations of neutral Fe layers and fast gravity waves in the thermosphere (110–155 km) at McMurdo (77.8 °S, 166.7 °E), Antarctica. Geophys. Res. Lett. 38, L23807. http://dx.doi.org/10.1029/2011GL050016.
Chu, X., Huang, W., Fong, W., Yu, Z., Wang, Z., Smith, J.A., Gardner, C.S., 2011b. First lidar observations of polar mesospheric clouds and Fe temperatures at McMurdo (77.8 °S, 166.7 °E), Antarctica. Geophys. Res. Lett. 38, L16810. http://dx.doi.org/10.1029/2011GL048373.
Chui, C.K., 1992. An Introduction to Wavelets, Wavelet Analysis and Its Applications. Academic Press, San Diego, CA. http://dx.doi.org/10.1016/B978-0-12-174584-4.50001-3.
Collins, R.L., Tao, X., Gardner, C.S., 1996. Gravity wave activity in the upper mesosphere over Urbana, Illinois: lidar observations and analysis of gravity wave propagation models. J. Atmos. Terr. Phys. 58, 1905–1926. http://dx.doi.org/10.1016/0021-9169(96)00026-8.
Daubechies, I., 1992. Ten Lectures on Wavelets. Society for Industrial and Applied Mathematics, Philadelphia, Pennsylvania. http://dx.doi.org/10.1137/1.9781611970104.
Daubechies, I., 1988. Orthonormal bases of compactly supported wavelets. Commun. Pure Appl. Math. 41, 909–996. http://dx.doi.org/10.1002/cpa.3160410705.
Farge, M., 1992. Wavelet transforms and their applications to turbulence. Annu. Rev. Fluid Mech. 24, 395–457. http://dx.doi.org/10.1146/annurev.fl.24.010192.002143.
Farge, M., Holschnerider, M., Colonna, J.F., 1990. Wavelet analysis of coherent structures in two-dimensional trubulent flows. In: Moffatt, H.K., Tsinober, A. (Eds.), Topological Fluid Mechanics: Proceedings of the IUTAM Symposium, Cambridge, UK, 13-18 August, 1989. Cambridge University Press, Cambridge, 765–776.
Forbes, J.M., 1995. Tidal and Planetary Waves. In: Johnson, R.M., Killeen, T.L. (Eds.), The Upper Mesosphere and Lower Thermosphere: A Review of Experiment and Theory, Geophysical Monograph Series. American Geophysical Union, Washington, D. C, 67–87. http://dx.doi.org/10.1029/GM087.
Forbes, J.M., Makarov, N.A., Portnyagin, Y.I., 1995. First results from the meteor radar at South Pole: a large 12-hour oscillation with zonal wavenumber one. Geophys. Res. Lett. 22, 3247–3250. http://dx.doi.org/10.1029/95GL03370.
Fritts, D.C., Alexander, M.J., 2012. Correction to “Gravity wave dynamics and effects in the middle atmosphere. Rev. Geophys. 50, RG3004. http://dx.doi.org/10.1029/2012RG000409.
Fritts, D.C., Alexander, M.J., 2003. Gravity wave dynamics and effects in the middle atmosphere. Rev. Geophys. 41, 1003. http://dx.doi.org/10.1029/2001RG000106.
Gardner, C.S., Miller, M.S., Liu, C.H., 1989. Rayleigh Lidar observations of gravity wave activity in the upper stratosphere at Urbana, Illinois. J. Atmos. Sci. 46, 1838–1854. http://dx.doi.org/10.1175/1520-0469(1989)046 < 1838:RLOOGW > 2.0.CO;2.
Gardner, C.S., Voelz, D.G., 1987. Lidar studies of the nighttime sodium layer over Urbana, Illinois: 2. Gravity waves. J. Geophys. Res. 92, 4673–4694. http://dx.doi.org/10.1029/JA092iA05p04673.
Gong, J., Yue, J., Wu, D.L., 2015. Global survey of concentric gravity waves in AIRS images and ECMWF analysis. J. Geophys. Res. Atmos. 120, 2210–2228. http://dx.doi.org/10.1002/2014JD022527.
Grossmann, A., Morlet, J., 1984. Decomposition of Hardy functions into square integrable wavelets of constant shape. SIAM J. Math. Anal. 15, 723–736. http://dx.doi.org/10.1137/0515056.
Guest, F.M., Reeder, M.J., Marks, C.J., Karoly, D.J., 2000. Inertia–gravity waves observed in the lower stratosphere over Macquarie Island. J. Atmos. Sci. 57, 737–752. http://dx.doi.org/10.1175/1520-0469(2000)057 < 0737:IGWOIT > 2.0.CO;2.
Hall, G.E., Meek, C.E., Manson, A.H., 1995. Hodograph analysis of mesopause region winds observed by three MF radars in the Canadian Prairies. J. Geophys. Res. 100, 7411–7421. http://dx.doi.org/10.1029/95JD00195.
Harris, T.J., 1994. A long-term study of the quasi-two-day wave in the middle atmosphere. J. Atmos. Terr. Phys. 56, 569–579. http://dx.doi.org/10.1016/0021-9169(94)90098-1.
Kaifler, B., Kaifler, N., Ehard, B., Dörnbrack, A., Rapp, M., Fritts, D.C., 2015. Influences of source conditions on mountain wave penetration into the stratosphere and mesosphere. Geophys. Res. Lett. 42, 9488–9494. http://dx.doi.org/10.1002/2015GL066465.
Kumar, P., 1995. A wavelet based methodology for scale-space anisotropic analysis. Geophys. Res. Lett. 22, 2777–2780. http://dx.doi.org/10.1029/95GL02934.
Kumar, P., Foufoula-Georgiou, E., 1997. Wavelet analysis for geophysical applications. Rev. Geophys. 35, 385–412. http://dx.doi.org/10.1029/97RG00427.
Liu, P.C., 1994. Wavelet spectrum analysis and ocean wind waves. In: Foufoula-Georgiou, E., Kumar, P. (Eds.), Wavelets in Geophysics, Wavelet Analysis and Its Applications. Academic Press, San Diego, CA, 151–166. http://dx.doi.org/10.1016/B978-0-08-052087-2.50012-8.
Liu, Y., San Liang, X., Weisberg, R.H., 2007. Rectification of the bias in the wavelet power spectrum. J. Atmos. Ocean. Technol. 24, 2093–2102. http://dx.doi.org/10.1175/2007JTECHO511.1.
Lu, X., Chen, C., Huang, W., Smith, J.A., Chu, X., Yuan, T., Pautet, P.-D., Taylor, M.J., Gong, J., Cullens, C.Y., 2015. A coordinated study of 1 h mesoscale gravity waves propagating from Logan to Boulder with CRRL Na Doppler lidars and temperature mapper. J. Geophys. Res. Atmos. 120, 10,006–10,021. http://dx.doi.org/10.1002/2015JD023604.
Mallat, S., 1999. A Wavelet Tour of Signal Processing 2nd ed. Elsevier, San Diego, CA. http://dx.doi.org/10.1016/B978-012466606-1/50000-3.
Mallat, S., 1989. A theory for multiresolution signal decomposition: the wavelet representation. IEEE Trans. Pattern Anal. Mach. Intell. 11, 674–693. http://dx.doi.org/10.1109/34.192463.
Manson, A., Meek, C., 1986. Dynamics of the middle atmosphere at Saskatoon (52 °N, 107 °W): a spectral study during 1981, 1982. J. Atmos. Terr. Phys. 48, 1039–1055. http://dx.doi.org/10.1016/0021-9169(86)90025-5.
Mayr, H.G., Mengel, J.G., Talaat, E.R., Porter, H.S., Chan, K.L., 2004. Properties of internal planetary-scale inertio gravity waves in the mesosphere. Ann. Geophys. 22, 3421–3435. http://dx.doi.org/10.5194/angeo-22-3421-2004.
Meyer, Y., 1989. Orthonormal wavelets. In: Combes, J.-M., Grossmann, A., Tchamitchian, P. (Eds.), Wavelets: Time-Frequency Methods and Phase Space. Springer Berlin Heidelberg, Berlin, Heidelberg, 21–37. http://dx.doi.org/10.1007/978-3-642-97177-8_2.
Meyer, Y., Salinger, D.H., 1993. Wavelets and Operators 1st ed. Cambridge University Press, Cambridge. http://dx.doi.org/10.1017/CBO9780511623820.
Meyers, S.D., Kelly, B.G., O'Brien, J.J., 1993. An introduction to wavelet analysis in oceanography and meteorology: with application to the dispersion of Yanai Waves. Mon. Weather Rev. 121, 2858–2866. http://dx.doi.org/10.1175/1520-0493(1993)121 < 2858:AITWAI > 2.0.CO;2.
Morlet, J., Arens, G., Fourgeau, E., Giard, D., 1982a. Wave propagation and sampling theory—part I: complex signal and scattering in multilayered media. GEOPHYSICS 47, 203–221. http://dx.doi.org/10.1190/1.1441328.
Morlet, J., Arens, G., Fourgeau, E., Giard, D., 1982b. Wave propagation and sampling theory—part II: sampling theory and complex waves. GEOPHYSICS 47, 222–236. http://dx.doi.org/10.1190/1.1441329.
Murenzi, R., 1989. Wavelet transforms associated to the n-dimensional Euclidean group with dilations: signal in more than one dimension. In: Combes, J.-M., Grossmann, A., Tchamitchian, P. (Eds.), Wavelets: Time-Frequency Methods and Phase Space. Springer Berlin Heidelberg, Berlin, Heidelberg, 239–246. http://dx.doi.org/10.1007/978-3-642-97177-8_22.
Nakamura, T., Tsuda, T., Yamamoto, M., Fukao, S., Kato, S., 1993. Characteristics of gravity waves in the mesosphere observed with the middle and upper atmosphere radar: 2. Propagation direction. J. Geophys. Res. 98, 8911–8923. http://dx.doi.org/10.1029/92JD03030.
Nastrom, G.D., Eaton, F.D., 2006. Quasi-monochromatic inertia-gravity waves in the lower stratosphere from MST radar observations. J. Geophys. Res. 111, D19103. http://dx.doi.org/10.1029/2006JD007335.
Nicolls, M.J., Varney, R.H., Vadas, S.L., Stamus, P.A., Heinselman, C.J., Cosgrove, R.B., Kelley, M.C., 2010. Influence of an inertia-gravity wave on mesospheric dynamics: a case study with the Poker Flat Incoherent Scatter Radar. J. Geophys. Res. 115, D00N02. http://dx.doi.org/10.1029/2010JD014042.
Pancheva, D., Mitchell, N., Clark, R.R., Drobjeva, J., Lastovicka, J., 2002. Variability in the maximum height of the ionospheric F2-layer over Millstone Hill (September 1998–March 2000); influence from below and above. Ann. Geophys. 20, 1807–1819. http://dx.doi.org/10.5194/angeo-20-1807-2002.
Paul, T., 1984. Functions analytic on the half-plane as quantum mechanical states. J. Math. Phys. 25, 3252–3263. http://dx.doi.org/10.1063/1.526072.
Pautet, P.-D., Taylor, M.J., Fritts, D.C., Bossert, K., Williams, B.P., Broutman, D., Ma, J., Eckermann, S.D., Doyle, J.D., 2016. Large-amplitude mesospheric response to an orographic wave generated over the Southern Ocean Auckland Islands (50.7 °S) during the DEEPWAVE project. J. Geophys. Res. Atmos. 121, 1431–1441. http://dx.doi.org/10.1002/2015JD024336.
Sato, K., 1994. A statistical study of the structure, saturation and sources of inertio-gravity waves in the lower stratosphere observed with the MU radar. J. Atmos. Terr. Phys. 56, 755–774. http://dx.doi.org/10.1016/0021-9169(94)90131-7.
Sato, K., O'Sullivan, D.J., Dunkerton, T.J., 1997. Low-frequency inertia-gravity waves in the stratosphere revealed by three-week continuous observation with the MU radar. Geophys. Res. Lett. 24, 1739–1742. http://dx.doi.org/10.1029/97GL01759.
Sato, K., Watanabe, S., Kawatani, Y., Tomikawa, Y., Miyazaki, K., Takahashi, M., 2009. On the origins of mesospheric gravity waves. Geophys. Res. Lett. 36, L19801. http://dx.doi.org/10.1029/2009GL039908.
Sato, K., Yamada, M., 1994. Vertical structure of atmospheric gravity waves revealed by the wavelet analysis. J. Geophys. Res. 99, 20623–20631. http://dx.doi.org/10.1029/94JD01818.
Sato, K., Yoshiki, M., 2008. Gravity wave generation around the polar vortex in the stratosphere revealed by 3-hourly radiosonde observations at Syowa Station. J. Atmos. Sci. 65, 3719–3735. http://dx.doi.org/10.1175/2008JAS2539.1.

She, C.Y., Li, T., Collins, R.L., Yuan, T., Williams, B.P., Kawahara, T.D., Vance, J.D., Acott, P., Krueger, D.A., Liu, H.-L., Hagan, M.E., 2004. Tidal perturbations and variability in the mesopause region over Fort Collins, CO (41N, 105W): continuous multi-day temperature and wind lidar observations. Geophys. Res. Lett. 31, L24111. http://dx.doi.org/10.1029/2004GL021165.

Shibuya, R., Sato, K., Tomikawa, Y., Tsutsumi, M., Sato, T., 2015. A study of multiple tropopause structures caused by inertia–gravity waves in the Antarctic. J. Atmos. Sci. 72, 2109–2130. http://dx.doi.org/10.1175/JAS-D-14-0228.1.

Taylor, M.J., Gu, Y.Y., Tao, X., Gardner, C.S., Bishop, M.B., 1995. An investigation of intrinsic gravity wave signatures using coordinated lidar and nightglow image measurements. Geophys. Res. Lett. 22, 2853–2856. http://dx.doi.org/10.1029/95GL02949.

Teitelbaum, H., Vial, F., 1991. On tidal variability induced by nonlinear interaction with planetary waves. J. Geophys. Res. 96, 14169–14178. http://dx.doi.org/10.1029/91JA01019.

Terradellas, E., Morales, G., Cuxart, J., Yagüe, C., 2001. Wavelet methods: application to the study of the stable atmospheric boundary layer under non-stationary conditions. Dyn. Atmos. Ocean. 34, 225–244. http://dx.doi.org/10.1016/S0377-0265(01)00069-0.

Torrence, C., Compo, G.P., 1998. A Practical Guide to Wavelet Analysis. Bull. Am. Meteorol. Soc. 79, 61–78. http://dx.doi.org/10.1175/1520-0477(1998)079 < 0061:APGTWA > 2.0.CO;2.

Vadas, S.L., 2007. Horizontal and vertical propagation and dissipation of gravity waves in the thermosphere from lower atmospheric and thermospheric sources. J. Geophys. Res. 112, A06305. http://dx.doi.org/10.1029/2006JA011845.

Vadas, S.L., Fritts, D.C., 2005. Thermospheric responses to gravity waves: influences of increasing viscosity and thermal diffusivity. J. Geophys. Res. 110, D15103. http://dx.doi.org/10.1029/2004JD005574.

Vaughan, G., Worthington, R.M., 2007. Inertia-gravity waves observed by the UK MST radar. Q. J. R. Meteorol. Soc. 133, 179–188. http://dx.doi.org/10.1002/qj.142.

Walterscheid, R.L., Hecht, J.H., Vincent, R. a., Reid, I. m., Woithe, J., Hickey, M.P., 1999. Analysis and interpretation of airglow and radar observations of quasi-monochromatic gravity waves in the upper mesosphere and lower thermosphere over Adelaide, Australia (35 °S, 138 °E). J. Atmos. Sol. Terr. Phys. 61, 461–478. http://dx.doi.org/10.1016/S1364-6826(99)00002-4.

Wang, N., Lu, C., 2010. Two-dimensional continuous wavelet analysis and its application to meteorological data. J. Atmos. Ocean. Technol. 27, 652–666. http://dx.doi.org/10.1175/2009JTECHA1338.1.

Wang, Z., Chu, X., Huang, W., Fong, W., Smith, J.A., Roberts, B., 2012. Refurbishment and upgrade of Fe Boltzmann/Rayleigh temperature lidar at Boulder for McMurdo lidar campaign in Antarctica, In: Proceedings of the 26th International Laser Radar Conference. Porto Heli, Greece, pp. 207–210.

Weng, H., Lau, K.-M., 1994. Wavelets, period doubling, and time–frequency localization with application to organization of convection over the Tropical Western Pacific. J. Atmos. Sci. 51, 2523–2541. http://dx.doi.org/10.1175/1520-0469(1994)051 < 2523:WPDATL > 2.0.CO;2.

Wickerhauser, M.V., 1994. Comparison of picture compression methods: wavelet, wavelet packet, and local cosine transform coding. In: Chui, C.K., Montefusco, L., Puccio, L. (Eds.), Wavelets: Theory, Algorithms, and Applications, Wavelet Analysis and Its Applications. Academic Press, San Diego, CA, 585–621. http://dx.doi.org/10.1016/B978-0-08-052084-1.50033-8.

Yu, Z., Chu, X., Huang, W., Fong, W., Roberts, B.R., 2012. Diurnal variations of the Fe layer in the mesosphere and lower thermosphere: four season variability and solar effects on the layer bottomside at McMurdo (77.8 °S, 166.7 °E), Antarctica. J. Geophys. Res. Atmos. 117, D22303. http://dx.doi.org/10.1029/2012JD018079.

Yuan, T., Heale, C.J., Snively, J.B., Cai, X., Pautet, P.-D., Fish, C., Zhao, Y., Taylor, M.J., Pendleton, W.R., Wickwar, V., Mitchell, N.J., 2016. Evidence of dispersion and refraction of a spectrally broad gravity wave packet in the mesopause region observed by the Na lidar and Mesospheric Temperature Mapper above Logan, Utah. J. Geophys. Res. Atmos. 121, 579–594. http://dx.doi.org/10.1002/2015JD023685.

Yue, J., Vadas, S.L., She, C.-Y., Nakamura, T., Reising, S.C., Liu, H.-L., Stamus, P., Krueger, D.A., Lyons, W., Li, T., 2009. Concentric gravity waves in the mesosphere generated by deep convective plumes in the lower atmosphere near Fort Collins, Colorado. J. Geophys. Res. 114, D06104. http://dx.doi.org/10.1029/2008JD011244.

Zhang, F.Q., Koch, S.E., Davis, C.A., Kaplan, M.L., 2001. Wavelet analysis and the governing dynamics of a large-amplitude mesoscale gravity-wave event along the East Coast of the United States. Q. J. R. Meteorol. Soc. 127, 2209–2245. http://dx.doi.org/10.1002/qj.49712757702.

Zhao, Y., Taylor, M.J., Randall, C.E., Lumpe, J.D., Siskind, D.E., Bailey, S.M., Russell, J.M., 2015. Investigating seasonal gravity wave activity in the summer polar mesosphere. J. Atmos. Sol. Terr. Phys. 127, 8–20. http://dx.doi.org/10.1016/j.jastp.2015.03.008.

Zink, F., Vincent, R.A., 2001. Wavelet analysis of stratospheric gravity wave packets over Macquarie Island: 1. Wave parameters. J. Geophys. Res. 106, 10275–10288. http://dx.doi.org/10.1029/2000JD900847.